Elastic Contrast, Rupture Directivity, and Damage Asymmetry in an Anisotropic Bimaterial Strike-Slip Fault at Middle Crustal Depths

Bo Ra Song[1]*, Won Joon Song[1], Scott E. Johnson[1], Christopher C. Gerbi[1], Senthil S. Vel[2]

[1]School of Earth and Climate Sciences, University of Maine, Orono, Maine 04469, USA.
[2]Department of Mechanical Engineering, University of Maine, Orono, Maine 04469, USA.
*Corresponding author: Bo Ra Song (bora.song@maine.edu)

Key Points:

- Seismic properties are analyzed for two anisotropic rocks with different mica content across a strike-slip fault showing asymmetric damage
- Horizontally polarized shear wave propagating parallel to the fault is important in determining elastic contrast between these rocks
- Calculating elastic contrast from the horizontal shear wave in these rocks leads to results consistent with models in isotropic media

Abstract

Mature faults with large cumulative slip often separate rocks with dissimilar elastic properties and show asymmetric damage distribution. Elastic contrast across such bimaterial faults can significantly modify various aspects of earthquake rupture dynamics, including normal stress variations, rupture propagation direction, distribution of ground motions, and evolution of off-fault damage. Thus, analyzing elastic contrasts of bimaterial faults is important for understanding earthquake physics and related hazard potential. The effect of elastic contrast between isotropic materials on rupture dynamics is relatively well studied. However, most fault rocks are elastically anisotropic, and little is known about how the anisotropy affects rupture dynamics. We examine microstructures of the Sandhill Corner shear zone, which separates quartzofeldspathic rock and micaceous schist with wider and narrower damage zones, respectively. This shear zone is part of the Norumbega fault system, a Paleozoic, large-displacement, seismogenic, strike-slip fault system exhumed from middle crustal depths. We calculate elastic properties and seismic wave speeds of elastically anisotropic rocks from each unit having different proportions of mica grains aligned sub-parallel to the fault. Our findings show that the horizontally polarized shear wave propagating parallel to the bimaterial fault (with fault-normal particle motion) is the slowest owing to the fault-normal compliance and therefore may be important in determining the elastic contrast that affects rupture dynamics in anisotropic media. Following results from subshear rupture propagation models in isotropic media, our results are consistent with ruptures preferentially propagated in the slip direction of the schist, which has the slower horizontal shear wave and larger fault-normal compliance.

Plain Language Summary

Earthquake faults that separate geologic materials with different elastic properties are referred to as bimaterial faults. Elastic contrast across bimaterial faults can modify rupture dynamics including rupture propagation direction and earthquake intensity and is therefore important for understanding potential earthquake hazards. The effects of elastic contrast between elastically isotropic materials (same elastic properties in all directions) on rupture propagation are reasonably well understood. However, rocks separated by natural faults are typically elastically anisotropic (having different elastic properties in different directions), and we know relatively little about the effects of this anisotropy on rupture propagation. To better understand the effects of elastic anisotropy, we analyze anisotropic rocks with different mica proportions collected from both sides of an ancient strike-slip earthquake fault, in which mica grains are aligned sub-parallel to the fault. We calculate the velocities of seismic waves in these rocks and their elastic contrast. We find that analysis of the horizontal shear wave propagating parallel to the subvertical fault plane gives results that are consistent with rupture propagation theory for isotropic materials. Thus, the shear-wave propagation direction should be considered when measuring seismic velocities and calculating elastic contrasts to investigate rupture along natural faults in anisotropic rocks.

Index Terms

7203 Body waves; 7209 Earthquake dynamics; 8010 Fractures and faults; 8030 Microstructures; 8118 Dynamics and mechanics of faulting

Keywords

asymmetric damage distribution; bimaterial fault; EBSD; elastic contrast; rupture directivity; seismic anisotropy

1. Introduction

A bimaterial interface separating different materials is common along mature faults. Examples include strike-slip faults separating tectonic plates with different rock types (e.g., Allam et al., 2014), subduction zones separating continental and oceanic crust (e.g., Turcotte & Schubert, 2014), and in the context of glacial earthquakes, ice-rock interfaces at the base of glaciers (e.g., Danesi et al., 2007; Weertman, 2005). When considering strike-slip faults, rupture along a bimaterial interface is fundamentally different from rupture along a homogeneous interface (e.g., Adams, 1995; Ampuero & Ben-Zion, 2008; Andrews & Ben-Zion, 1997; Brener et al., 2016; Rice et al., 2001; Shi & Ben-Zion, 2006; Weertman, 1980). On a planar interface in a homogeneous isotropic medium bounded by similar materials with identical elastic stiffness and density, the shear source radiation moves with a symmetric disturbance in both sides of the interface. In this case, no coupling occurs between shear slip and normal stress on the interface, and therefore no change in normal stress occurs on the interface (Figure 1a; e.g., Ben-Zion, 2001). In contrast, for an isotropic bimaterial planar interface bounded by materials with different elastic stiffness and density, the symmetry of the near-tip stress and displacement fields across the interface are broken (Figure 1b; e.g., Ben-Zion, 2001). As a result, variations of normal stress are theoretically expected to couple to perturbations of in-plane slip on the interface (“bimaterial coupling”). Due to the bimaterial coupling in mode II (in-plane shear) ruptures, the sense of normal stress variation on the interface during propagation in one direction is reverse of the sense in the opposite direction. For a standard subshear rupture propagating in the slip direction of the more compliant material (so-called “positive” direction), normal stress can be dynamically reduced near the rupture tip. This normal stress reduction produces dilation and spatially localized pulse-like slip at the leading edge of the rupture tip, facilitating rupture propagation (Figures 1b and c; e.g., Andrews & Ben-Zion, 1997; Ben-Zion & Huang, 2002; Weertman, 1980). In the opposite “negative” direction (the slip direction of the stiffer material) of a subshear rupture, dynamic increase in normal stress at the trailing edge of the rupture tip causes compression that arrests the slip motion behind the rupture front, suppressing rupture propagation in the negative direction (Figure 1c; e.g., Ampuero & Ben-Zion, 2008; Shi & Ben-Zion, 2006). For these reasons, rupture propagation during bimaterial rupture is expected to be predominantly unidirectional (e.g., Ampuero & Ben-Zion, 2008; Andrews & Ben-Zion, 1997; Dalguer & Day, 2009; Erickson & Day, 2016; Xu & Ben-Zion, 2017).

Preferred rupture propagation (or rupture directivity) along bimaterial faults is of great interest in seismology and earthquake engineering communities because of its effect on near-fault ground motions (e.g., Brietzke et al., 2009). In near-field regions of bimaterial faults, the subshear rupture propagating in a positive direction generates pulse-like ground motions from shear waves characterized by large amplitudes, long periods, and short durations (e.g., Bernard et al., 1996; Bertero et al., 1978; Boatwright & Boore, 1982; Yazdani et al., 2017; Zhai et al., 2018). These motions are distinct from ordinary non-pulse-like ground motions that are commonly observed in far-field regions. An important feature of the impulsive shear-wave motions is large particle displacements normal to the fault relative to those parallel to the fault (Figure 1c; e.g., Ben-Zion, 2001; Somerville et al., 1997). Moreover, the long-period average pulse-like motions in both fault-normal and fault-parallel directions in the near field are more intense than the far-field motions (e.g., Bray et al., 2009). Consequently, the pulse-like near-field ground motions in the positive direction of bimaterial faults are potentially more destructive and can cause serious damage to human-made structures (e.g., Champion & Liel, 2012; Hall et al., 1995; Kalkan & Kunnath, 2006). Therefore, accurately predicting rupture directivity and resultant ground motions are of growing importance for estimating the seismic hazard near faults.

Rupture directivity also influences the distribution of off-fault rock damage. Ruptures in a homogeneous isotropic medium that propagate bilaterally without a preferred direction produce rock damage (tensile fractures at high angle to the fault) primarily in the two tensile quadrants of the radiated seismic field (Figure 1d; e.g., Ben-Zion & Shi, 2005; Dalguer et al., 2003; Griffith et al., 2009; Okubo et al., 2019; Thomas et al., 2017; Thomas & Bhat, 2018; Xu & Ben-Zion, 2017). Thus, a relatively symmetrical distribution of damage is expected around the homogeneous fault after multiple rupture events with different hypocenter locations. In contrast, the cumulative effect of multiple rupture propagation events with a preferred direction along isotropic bimaterial faults generates asymmetric damage, with more damage on the stiffer side of the fault, or in the tensile quadrant for each wrinkle-like pulse propagating in the positive direction (Figure 1e; e.g., Ben-Zion & Shi, 2005; Xu & Ben-Zion, 2017). Highly fractured and pulverized rocks in the damage zones of bimaterial faults typically exhibit tensile microfractures with little apparent preferred orientation (Figure 1e; e.g., Rempe et al., 2013; Xu & Ben-Zion, 2017).

In the above context, analyzing contrasts in elastic and seismic properties of bimaterial faults is an important step towards a better understanding of rupture directivity and related hazard potential. In elastically isotropic media, the effect of elastic contrast between two different materials (e.g., bimaterial coupling) is relatively well studied through theoretical and numerical experiments (e.g., Adda-Bedia & Ben Amar, 2003; Ampuero & Ben-Zion, 2008; Andrews & Ben-Zion, 1997; Cochard & Rice, 2000; Weertman, 1980). However, most crustal rocks are elastically anisotropic and show seismic anisotropy, or directional dependence of seismic velocity (e.g., Almqvist & Mainprice, 2017; Babuška & Cara, 1991; Christensen & Mooney, 1995). The anisotropy causes change of elastic contrast between natural rocks depending on direction, and even a switch of relative strength (e.g., from stiffer to more compliant rock) might occur at certain directions. Although some workers investigated damage asymmetry in natural bimaterial faults and discussed their preferred rupture propagation directions (e.g., Dor et al., 2008; Dor, Ben-Zion, et al., 2006; Dor, Rockwell, et al., 2006; Mitchell et al., 2011; Rempe et al., 2013; B. R. Song et al., 2020), they did not analyze elastic or seismic contrast of the anisotropic rocks. In the present study, we investigate potential effects of elastic contrast (represented by difference in seismic wave velocity) on rupture directivity and damage distribution in bimaterial faults/shear zones separating dissimilar and elastically anisotropic rocks. We calculate elastic properties and seismic wave velocities of two anisotropic rocks (quartzofeldspathic rock and mica-rich schist) juxtaposed across the deeply exhumed, seismogenic Sandhill Corner shear zone, an ancient strike-slip fault that exhibits strongly asymmetric damage distribution (B. R. Song et al., 2020). We determine elastic contrast of the anisotropic rocks and conclude that the horizontally polarized shear wave propagating parallel to the fault may be the most relevant wave to consider when comparing our results to isotropic bimaterial rupture models. To further explore and generalize our results, synthetic microstructures with mica preferred orientation are used to conduct sensitivity analysis on the effect of modal mineralogy (i.e., mica proportion from 0% to 100%) on seismic contrast and rupture directivity. We compare our results of seismic anisotropy and contrast to published data of other natural rocks with various mica contents.

2. The Sandhill Corner shear zone of the Norumbega fault system

2.1. Geologic setting

The Sandhill Corner shear zone (SCSZ) is located in the south-central portion of the Norumbega fault system in the northeastern Appalachians of the North America (Figure 2a).

Field and geochronological studies suggest that the Norumbega fault experienced regional scale, orogeny-parallel, dextral strike-slip shear deformation in the late Paleozoic (Ludman et al., 1999; Wang & Ludman, 2004; West, 1999). Although the total displacement along the fault system is uncertain, estimates of 25–300 km have been reported on the basis of the map relations and shear strain analysis (Hubbard, 1999; Swanson, 1992; Wang & Ludman, 2004). The Norumbega fault spans a length of nearly 450 km from southwestern Maine, USA to central New Brunswick, Canada (Figure 2a; e.g., Hussey, 1988; Hussey et al., 1986; Ludman, 1998; Newberg, 1985; Pankiwskyj, 1996; Swanson, 1992; Swanson et al., 1986) and possibly extends up to ~1200 km from Connecticut, USA to the Gulf of St. Lawrence, Canada (Figure 2a; Goldstein & Hepburn, 1999; Ludman, 1998), comparable to the overall length of the San Andreas fault, California, USA. Seismic reflection profiles suggest that strands of the Norumbega fault crosscut the Moho (e.g., Doll et al., 1996).

The SCSZ in the study area (Figures 2a and b) is a ~230 m wide shear zone that contains quartz- and feldspar-rich mylonitic rocks of the Cape Elizabeth Formation on the northwest side and sheared schist of the Crummett Mountain Formation on the southeast side (Grover & Fernandes, 2003; Price et al., 2016; West & Peterman, 2004), and thus can be referred to as a bimaterial fault/shear zone. Pseudotachylyte is observed within ~40 m of the shear zone core in the quartzofeldspathic (QF) rocks and within ~5 m of the core in the schist (Price et al., 2012; W. J. Song et al., 2020). The mylonitic foliation of the SCSZ is subvertical and northeast-trending, having subhorizontal stretching lineation (Figure 2c). The QF and schist host rocks show sub-parallel foliation to that of the SCSZ (Figure 2c). The seismogenic parts of the shear zone were active at temperature of 350–500 °C (Price et al., 2016), indicating it was exhumed form middle crustal depths. Mean kinematic vorticity number of 0.97 and microstructures of shear bands, muscovite fish and mantled feldspar porphyroclasts in the SCSZ reveals approximately strike-slip flow with dextral sense of shear (Johnson et al., 2009; West & Hubbard, 1997).

2.2. Asymmetric damage distribution

Rocks within the SCSZ contain highly fractured and fragmented garnet grains. B. R. Song et al. (2020) analyzed the width of effective damage either side of the lithologic contact/shear-zone core based on the microfracture density measurements of the fractured or fragmented garnets. The damage distribution is highly asymmetric: ~207 m and ~53 m wide in the QF and schist units, respectively (Figure 2d). Using fragment size distribution analysis with three-dimensional *D*-value greater than 2.5, the boundaries between fractured and pulverized zones are located at ~63 m in the QF and ~5 m in the schist unit from the lithologic contact, indicating highly asymmetric distribution of pulverized zones as well (Figure 2d; B. R. Song et al., 2020). The wider pulverized zone determined by fragmented garnet in the QF unit is comparable to the dynamic strain-rate region (~60 m wide) determined by muscovite kink-band geometries (Anderson et al., 2021) and the coseismic damage zone (~90 m wide) determined by spatial abundance of fluid inclusions in the QF rocks (W. J. Song et al., 2020). Johnson, Song, Vel, et al. (2021) have summarized these relations and their implications for energy expenditure in the earthquake source.

3. Methods

3.1. Sample selection

One representative host-rock sample was chosen from either side of the SCSZ (BB6 and 35) to estimate elastic and seismic properties of the shear zone (Figures 2b and 3). The QF and schist host rocks have the same major minerals with quartz + feldspars + biotite + muscovite > ~90 modal%. The protomylonite and mylonite in the shear zone were derived from the QF host rock, and all share a similar mineralogy with only varying minor accessory minerals. Mica-rich schist that has a planar foliation defined by alternating mica-rich and quartz/feldspar-rich layers is the protolith of sheared schist in the shear zone. We compare elastic properties of the host rocks as they best represent the initial or early states of the bimaterial contact in development of the shear zone. A more accurate representation of the elastic properties could be determined by averaging the measured elastic properties of multiple host-rock samples on either side of the shear zone core, but results from the selected samples are adequate for our purposes in the present study. Although it would be informative to assess the elastic properties of the highly strained mylonitic/ultramylonitic rocks adjacent to the shear-zone core, we are unable to do so using electron backscatter diffraction (EBSD) methods owing to the very fine grain size of mica and other minerals (a few microns to submicron in size). The QF/schist contact continues for ~5.8 km to the NE and >~6.2 km to the SW from the study area (Figure 2a). The full length of the contact to the SW is unknown due to lack of outcrop. Thus, we are confident that the damage distribution evaluated herein reflects the elastic contrast between these two units as opposed to being inherited from some earlier part of the displacement history.

To help interpretation of seismic velocities for the complex natural samples, we also generate two simplified synthetic microstructures by changing the crystal orientations, pixel coordinates and phase information, as described by Naus-Thijssen, Goupee, Vel, et al. (2011). These synthetic microstructures have nearly identical modal mineral abundance to the natural rock samples. The synthetic microstructures contain quartz, plagioclase, biotite and muscovite. The quartz and plagioclase grains have hexagonal shape and random crystallographic orientation while the rectangular mica grains show strong preferred shape and c-axis orientations parallel and perpendicular to the foliation, respectively. Specifically, the basal (001) planes of mica grains are oriented with a mean angle of zero degrees with respect to both the $x1$ (lineation direction) and $x3$ (direction parallel to the foliation and perpendicular to the lineation) axes with deviation angle of ±10° (see Figure S1 for the coordinate system), but the [100] and [010] axes of mica are randomly oriented within the basal (001) planes. All grains/phases in the synthetic microstructures are randomly distributed in the $x1$-$x2$ coordinate plane.

3.2. Data acquisition and post-processing

Thin sections of the two natural samples from the QF and schist host rocks (Figure 3) were cut perpendicular to the local foliation and parallel to the local stretching lineation, which are sub-parallel to the lithologic contact/shear-zone core. They were polished with colloidal silica suspension for >2 hours before applying a thin carbon coat. EBSD patterns of the two samples were collected using a Tescan Vega II scanning electron microscope equipped with an EDAX-TSL EBSD system at the University of Maine, USA. Working conditions were 20 kV acceleration voltage, 70° sample tilt, and 25 mm working distance. EDAX-TSL OIM Data Collection 5.31 software was used to index EBSD patterns on square grids with step size of 5 μm and 2 μm for relatively coarse-grained QF and fine-grained schist samples, respectively. Raw indexing rates were >94%.

EBSD data were post-processed with EDAX-TSL OIM Analysis 5.31 software to produce clean EBSD maps for the purpose of numerical analysis, following the procedure suggested in Johnson, Song, Cook, et al. (2021). They were reindexed to accurately identify phases using Hough peaks and chemistry, and to eliminate minor accessory phases (<5 modal%).

Non- and poorly-indexed pixels (<confidence index of 0.02) were replaced with well-indexed neighboring pixels. The well-indexed pixels are 86% and 61% of the EBSD maps for the QF and schist rocks, respectively. In order to produce perfectly bonded grain boundaries and uniform crystallographic orientation within a grain domain required for calculation of elastic properties using a finite element mesh, empty pixels (e.g., grain boundaries or eliminated minor phases) were filled with neighboring phases, twins in quartz and plagioclase were removed, and all pixels within a grain (with an internal misorientation <10°) were replaced by the average orientation for the grain. Finally, partially mis-indexed biotite and muscovite were manually corrected using a pseudosymmetry cleanup routine, comparing EBSD maps and photomicrographs.

3.3. Calculation of elastic and seismic properties

To quantitatively determine bulk stiffness tensors and seismic wave velocities from the cleaned EBSD maps, the Euler angles, pixel coordinates and phase information were used in the TESA (Thermo-Elastic and Seismic Analysis) numerical toolbox featuring a MATLAB-based graphical user interface (Figure S1a; Cook et al., 2018; Johnson, Song, Cook, et al., 2021). The TESA toolbox was developed by Cook et al. (2018) to investigate seismic anisotropy of rocks, but also calculates grain-scale mechanical and thermal stresses and thermal conductivity for polyphase aggregates. The software is based on the asymptotic expansion homogenization (AEH) method in conjunction with the finite element method that is useful for accurately calculating the homogenized elastic properties and computing seismic wave velocities in heterogeneous materials (Almqvist & Mainprice, 2017; Cyprych et al., 2017; Naus-Thijssen, Goupee, Vel, et al., 2011; Vel et al., 2016). The AEH method captures the heterogeneous grain-scale stress and strain distributions in a polycrystalline sample by accounting for elastic interactions between the grains (Vel et al., 2016). The homogenized stiffness tensors were computed using the elastic properties of trigonal α-quartz (Ohno et al., 2006), triclinic plagioclase (An25; Brown et al., 2016), monoclinic phlogopite (Chheda et al., 2014) for biotite, and monoclinic muscovite (Vaughan & Guggenheim, 1986). We note that biotite stiffness published by Aleksandrove & Ryzhova (1961) was not used because it assumes hexagonal symmetry. In the remainder of the paper when we refer to elastic properties of biotite, we use the elastic properties of phlogopite from Chheda et al. (2014). All four minerals are elastically anisotropic, and their single-crystal seismic properties are presented in Figure S2.

After homogenization analysis, we plot 3D wave velocities (*V*) using equal-area, upper-hemisphere projection (Figure S1b) and compute seismic anisotropy (in percentage) by $A = 100 \times (V_{\max} - V_{\min})/\left(0.5 \times (V_{\max} + V_{\min})\right)$. Using homogenized stiffness tensors, bulk densities, and the Christoffel equations (Christoffel, 1877), we calculate and plot 2D velocities of the compressional wave (*P* wave) and two shear waves (*SH* and *SV* waves; see Figure S3 for polarization) for incidence angles (azimuth ϕ) between 0° and 180° with 1° interval in the horizontal plane ($x1$-$x2$ plane in Figure S1c). These velocities are used to investigate contrasts in the velocities of different seismic waves, as a proxy for elastic contrast. In an anisotropic medium, *P* and *S* waves generally have quasi-compressional (qV_{P}) and quasi-shear (qV_{SH} and qV_{SV}) wave velocities since particle motion is neither exactly parallel nor perpendicular to the symmetry axis for most angles of incidence (e.g., Auld, 1990; Winterstein, 1990). The seismic velocity contrast (in percentage) between two rocks at a particular incidence angle is calculated as $100 \times |V_{\mathrm{rock1}} - V_{\mathrm{rock2}}|/\left(0.5 \times (V_{\mathrm{rock1}} + V_{\mathrm{rock2}})\right)$. The synthetic microstructures were similarly analyzed for elastic and seismic properties using the TESA toolbox.

4. Results

4.1. Microstructures of the quartzofeldspathic (QF) and schist units

Two natural rock samples from the QF (sample BB6) and schist (sample 35) units are composed primarily of quartz, plagioclase, biotite and muscovite, with minor garnet (Figure 3). In the selected regions for EBSD analysis (Figure 4a), quartz and plagioclase show coarse grains up to millimeter scale in the QF sample (averaging 101.1 and 121.9 μm, respectively) but relatively fine grains in the mica-rich schist (averaging 24.6 and 32.1 μm, respectively). In the QF rock with relatively low mica content (13.9 modal%), biotite has large grain size (average 84.6 μm) compared to the schist and exhibits a preferred orientation of its basal (001) planes sub-parallel to the shear-zone core or foliation (the $x1$-$x3$ plane) although biotite layering anastomoses around plagioclase grains (Figures 3a, 4a and S4a). Muscovite comprises a very small portion (0.5 modal%) of the QF rock (Figure 4a). Owing to their large grain size, quartz and plagioclase in the QF rock show similar degrees of crystallographic preferred orientation to biotite (Figure S4a). In the schist with high mica content (70.5 modal%), both biotite and muscovite grain sizes are relatively small (averaging 29.0 and 20.9 μm, respectively), and show strong preferred orientations of their basal (001) planes parallel to the foliation, whereas quartz and plagioclase have relatively weak crystallographic preferred orientations (Figures 4a and S4b).

4.2. Wave velocities and contrasts for the natural QF rock and schist

4.2.1. *P* wave

The 2D quasi-compressional wave velocities (qV_P) of the QF rock and schist in the horizontal $x1$-$x2$ plane are plotted as a function of azimuth ϕ in Figure 4b, using the homogenized stiffness tensors and densities computed by the TESA toolbox. qV_P at ϕ = 0° (or 180°) and ϕ = 90°, hereafter referred to as qV_P(0°) and qV_P(90°), represent a compressional wave velocity propagating, respectively, parallel and perpendicular to the strike of the SCSZ (the $x1$ direction). The QF rock with low mica content shows only a small variation in qV_P and thus low *P*-wave anisotropy in the $x1$-$x2$ plane (Figure 4b; see Table S1). In contrast, the schist with high mica content shows significant *P*-wave anisotropy in the $x1$-$x2$ plane. The schist qV_P showing the highest value at ϕ = 3° decreases with increasing ϕ and reaches its minimum value at ϕ = 96°, and its maximum difference is more than 2 km/s (Figure 4b; Table S1). Unlike the QF rock, the qV_P curve for the schist in the $x1$-$x2$ plane is approximately symmetrical with respect to ϕ = ~90° (Figure 4b). In the SCSZ-parallel direction, qV_P(0°) of the schist is faster than that of the QF rock, whereas in the SCSZ-perpendicular direction, the schist shows slower qV_P(90°) than the QF rock (Figure 4b).

Since the QF rock and schist show different degrees of seismic anisotropy in the $x1$-$x2$ plane, the *P*-wave velocity contrast between the two rocks varies with azimuth ϕ (Figure 4c). The qV_P contrast in the SCSZ ranges from 0% at the velocity crossovers to 17.6%, and the more compliant rock type (QF or schist) based on qV_P is also changed with ϕ (Figure 4c). The SCSZ-parallel and perpendicular qV_P contrasts at ϕ = 0° and ϕ = 90°, respectively, are 11.9% (more compliant QF) and 16.2% (more compliant schist).

The 3D qV_P for the QF and schist rocks is plotted in Figure 4d. Both rocks show minimum qV_P sub-perpendicular to the $x1$-$x3$ plane (foliation), but maximum and high qV_P in the QF rock is concentrated sub-parallel to the $x3$ direction, whereas the schist exhibits maximum and high qV_P along the foliation, displaying nearly hexagonal symmetry of *P*-wave velocity (Figure 4d). The *P*-wave seismic anisotropy of the schist (37.9%) is more than twice that of the

QF rock (15.3%) owing to the abundant mica with strong crystallographic preferred orientation (Figures 4d and S4b).

4.2.2. *S* waves

The 2D quasi-shear wave velocities with horizontal (qV_{SH}) and vertical (qV_{SV}) polarization of the QF and schist rocks are plotted as a function of azimuth ϕ in Figure 4e. The mica-poor QF rock shows only small variations in qV_{SH} and qV_{SV}, whereas the two *S* waves of the mica-rich schist have much larger seismic anisotropies in the $x1$-$x2$ plane (Figure 4e; see Table S1). In the schist, the slowest 2D qV_{SH} is present at $\phi = 3°$ with polarization sub-perpendicular to the foliation, and the fastest 2D qV_{SH} is at $\phi = 130°$ with neither polarization nor propagation (sub-)perpendicular to the foliation (Figure 4e; Table S1). 2D qV_{SV} of the schist is fastest at $\phi = 3°$ with both polarization and propagation (sub-)parallel to the foliation and slowest at $\phi = 93°$ with propagation sub-perpendicular to the foliation, and its maximum difference is more than 1 km/s (Figure 4e; Table S1). Unlike the QF rock, the schist has approximately symmetrical qV_{SH} and qV_{SV} patterns in the $x1$-$x2$ plane with respect to $\phi = {\sim}90°$ (Figure 4e). In the SCSZ-parallel direction, the schist shows faster $qV_{SV}(0°)$ than the QF rock, whereas in the SCSZ-perpendicular direction, $qV_{SV}(90°)$ of the schist is slower (Figure 4e). For qV_{SH} in the $x1$-$x2$ plane, the schist exhibits slower velocities than the QF rock at all azimuth angles except for $\phi = 126°$ to $130°$ where it is slightly faster than the QF rock (Figure 4e).

The seismic contrasts of *SH* and *SV* waves between the two rocks also varies with azimuth ϕ owing to different degrees of seismic anisotropy in the $x1$-$x2$ plane (Figure 4f). The qV_{SH} and qV_{SV} contrasts range from 0% to 29.8% and 26.0%, respectively. The qV_{SH} and qV_{SV} contrasts at $\phi = 0°$ are 25.5% (more compliant schist) and 11.5% (more compliant QF), respectively. At $\phi = 90°$, the contrasts of qV_{SH} and qV_{SV} are 21.0% and 25.9%, respectively, the schist being more compliant for both *SH* and *SV* waves (Figure 4f). Our analysis shows that, unlike elastically isotropic rocks, seismic wave velocities and their contrasts in anisotropic rocks depend on the incidence angle ϕ in the horizontal $x1$-$x2$ plane, and this will be discussed in Section 5.1.

The 3D qV_{SH} and qV_{SV} for the QF and schist rocks are plotted in Figures 4g and h where patterns of qV_{SH} and qV_{SV} in the mica-rich schist exhibit nearly hexagonal symmetry. In Figures

4g and h, the *SH*- and *SV*-wave seismic anisotropies of the mica-rich schist (42.6% and 39.8%, respectively) are more than twice those of the QF rock (15.0% and 18.7%, respectively).

4.3. Comparison with synthetic rock samples

Owing to the complex microstructures and seismic velocity patterns of the natural rocks (especially the QF rock), two simplified synthetic microstructures with nearly identical modal mineral abundance to the natural rocks were generated to better understand the effect of modal mineralogy on wave velocities and seismic anisotropy. The synthetic QF and schist samples have mica (biotite and muscovite) contents of 14.1% and 70.6%, respectively (Figure 5a).

4.3.1. *P* wave

Similar to the natural rocks, the 2D qV_P of the synthetic QF rock with low mica content shows small variation, whereas the synthetic schist with high mica content has significant qV_P variation more than 2 km/s in the horizontal $x1$-$x2$ plane (Figure 5b; see Table S1). For both synthetic rocks, the qV_P curves in the $x1$-$x2$ plane do not have minimum speeds in sub-perpendicular directions to the foliation close to $\phi = 90°$ (e.g., minimum at $\phi = 56°$ or 81°) while maximum velocities are shown in (sub-)parallel directions to the foliation close to $\phi = 0°$ or 180° (Figure 5b; Table S1). Owing to strong crystallographic preferred orientations in mica and nearly random orientations in quartz and plagioclase (Figure S5), these 2D velocity features for synthetic rocks are similar to the 2D qV_P for monoclinic biotite or muscovite single crystals plotted in the [100]-[001] plane (Figure S6). Interestingly, the qV_P curve for the mica-rich synthetic schist in the $x1$-$x2$ plane is approximately symmetrical with respect to $\phi = \sim 90°$ presumably due to a combination of the monoclinic velocity curves for biotite and muscovite (Figures 5b and S6). As with the natural rocks, the foliation-parallel $qV_P(0°)$ of the synthetic schist is faster than that of the synthetic QF rock, whereas in the foliation-perpendicular direction, the synthetic schist has slower $qV_P(90°)$ than the synthetic QF rock (Figure 5b).

The seismic contrast of *P* wave between the two synthetic rocks varies with azimuth ϕ owing to different degrees of their seismic anisotropies in the $x1$-$x2$ plane (Figure 5c), with values ranging from 0% to 18.6%. The foliation-parallel and perpendicular qV_P contrasts at $\phi = 0°$ and $\phi = 90°$ are 13.5% (more compliant synthetic QF) and 18.6% (more compliant synthetic schist), respectively (Figure 5c).

The 3D qV_P for the synthetic QF rock shows much simpler velocity pattern than the natural QF rock (Figure 5d), close to monoclinic symmetry of biotite in Figure S2. This simpler pattern reflects the random crystallographic orientations of synthetic quartz and plagioclase grains unlike the natural QF rock (Figure S5a). However, both natural and synthetic QF rocks show similar minimum and maximum qV_P and thus similar *P*-wave seismic anisotropies (15.3% and 12.0%, respectively; Figures 4d and 5d). The mica-rich synthetic schist displays approximately hexagonal symmetry of qV_P similar to the natural schist, considering maximum and high qV_P along the foliation owing to strong preferred orientation of the basal (001) planes of biotite and muscovite parallel to the foliation (Figures 5d and S5b). As in the natural rocks, Figure 5d shows the *P*-wave seismic anisotropy of the mica-rich synthetic schist (40.5%) is much higher than that of the synthetic QF rock (12.0%). The *P*-wave velocity comparison between the natural and synthetic rocks indicates that mica content and its crystallographic orientation are important factors in determining seismic velocities and anisotropy compared to the other minerals (quartz and plagioclase) because biotite and muscovite have much higher seismic anisotropies than quartz and plagioclase (Figure S2).

4.3.2. *S* waves

Similar to the natural rocks, 2D qV_{SH} and qV_{SV} of the synthetic mica-rich schist show much larger variations than the synthetic mica-poor QF rock in the $x1$-$x2$ plane (Figure 5e; see Table S1). For the synthetic QF and schist rocks, the slowest 2D qV_{SH} are present at $\phi = 174°$ and 90°, respectively, owing to its polarization or propagation (sub-)perpendicular to the foliation, and the fastest 2D qV_{SH} are present at $\phi = 42°$ and 55° with neither polarization nor propagation (sub-)perpendicular to the foliation (Figure 5e; Table S1). For qV_{SV} in the $x1$-$x2$ plane, as both polarization and propagation directions are (sub-)parallel to the foliation, the synthetic QF and schist rocks have maximum speeds at $\phi = 177°$ and 0°, respectively, and minimum speeds are present at $\phi = 97°$ and 95° with propagation sub-perpendicular to the foliation (Figure 5e; Table S1). These 2D velocity features for synthetic rocks are similar to the 2D qV_{SH} and qV_{SV} for monoclinic single-crystal biotite or muscovite plotted in the [100]-[001] plane (Figure S6), but the *S*-wave velocity curves for the mica-rich synthetic schist in the $x1$-$x2$ plane are approximately symmetrical with respect to $\phi = 90°$ presumably due to a combination of the monoclinic velocity curves for biotite and muscovite (Figure 5e). In the foliation-parallel direction, the synthetic schist shows faster $qV_{SV}(0°)$ than the synthetic QF rock, whereas in the foliation-perpendicular direction, $qV_{SV}(90°)$ of the synthetic schist is slower (Figure 5e). For qV_{SH} in the $x1$-$x2$ plane, the synthetic schist exhibits slower velocities than the synthetic QF rock at all azimuth angles (Figure 5e).

The seismic contrasts of *SH* and *SV* waves between the two synthetic rocks show similar variations with azimuth ϕ to the natural rocks (Figures 4f and 5f). The qV_{SH} contrast is between 4.1% and 23.4%, and the qV_{SV} contrast ranges from 0% to 24.4% (Figure 5f). The qV_{SH} and qV_{SV} contrasts at $\phi = 0°$ are 22.7% (more compliant synthetic schist) and 9.8% (more compliant synthetic QF), respectively. At $\phi = 90°$, the contrasts of qV_{SH} and qV_{SV} are 23.3% and 23.2%, respectively, the synthetic schist being more compliant for both *SH* and *SV* waves (Figure 5f).

Unlike the complicated velocity patterns of the natural QF rock, the 3D qV_{SH} and qV_{SV} patterns for the synthetic QF rock is similar to the monoclinic symmetry velocity patterns of single-crystal biotite, but its seismic anisotropies (16.4% for qV_{SH} and 15.6% for qV_{SV}) are comparable to the natural QF rock (Figures 5g, 5h and S2). The mica-rich synthetic schist shows nearly hexagonal symmetry of qV_{SH} and qV_{SV} similar to the natural schist and has much higher seismic anisotropies (47.0% for qV_{SH} and 46.8% for qV_{SV}) than the mica-poor synthetic QF rock (Figures 5g and h).

5. Discussion

5.1. Determination of elastic contrast between the anisotropic rocks

The effective damage zone around the SCSZ reveals asymmetric distribution being wider (~207 m) in the QF rocks and narrower (~53 m) in the schist, with similarly asymmetric distribution of pulverized zones of ~63 m and ~5 m in the QF and schist units, respectively (Figure 2d; B. R. Song et al., 2020). Asymmetric damage is commonly observed around bimaterial strike-slip faults separating rocks with different elastic properties (e.g., Dor et al., 2008; Dor, Ben-Zion, et al., 2006; Dor, Rockwell, et al., 2006; Mitchell et al., 2011; Rempe et al., 2013). Based on numerical rupture-propagation studies, the contrast in rock material properties across a fault leads to bimaterial coupling, which results in wrinkle-like pulse ruptures with unilateral rupture directivity in the slip direction of the more compliant side, and therefore produces asymmetry of ground motion and damage distribution due to the directivity effect (e.g., Ampuero & Ben-Zion, 2008; Andrews & Ben-Zion, 1997; Ben-Zion, 2001; Ben-Zion & Huang, 2002; Dalguer & Day, 2009; Erickson & Day, 2016; Shi & Ben-Zion, 2006; Weertman, 1980; Xu & Ben-Zion, 2017). Thus, determining elastic properties and wave-speed contrasts across the fault appears to be an integral component of understanding the rupture directivity and its related effects.

Owing to the difficulty of incorporating elastic anisotropy, numerical studies of rupture propagation typically treat rocks as elastically isotropic (Figure 1; e.g., Ampuero & Ben-Zion, 2008; Andrews & Ben-Zion, 1997; Brietzke et al., 2007; Cochard & Rice, 2000; Erickson & Day, 2016; Harris & Day, 1997; Shi & Ben-Zion, 2006; Xu & Ben-Zion, 2017). However, earthquake ruptures in natural faults typically occur in rocks with at least moderate elastic anisotropy, partly caused by rock fabrics and associated crystallographic preferred orientation developed during deformation-induced shearing and associated metamorphism (e.g., Audet, 2015; Christensen & Okaya, 2007; Jefferies et al., 2006; Li et al., 2014). In contrast to elastically isotropic rocks, anisotropic rocks show directional dependence of seismic wave velocities and thus velocity contrasts. For example, in the SCSZ-parallel direction at ϕ = 0°, the QF rock is more compliant for qV_P or qV_{SV} but the schist is more compliant for qV_{SH}. In contrast, the schist is more compliant for all three waves in the SCSZ-perpendicular direction at ϕ = 90° (Figures 4c and f). In this section, we discuss which elastic contrast between the two anisotropic rocks may be the most diagnostic for evaluating the potential for rupture directivity. Since it is difficult to visualize anisotropic elastic properties (e.g., stiffness tensor), we use seismic wave velocities and their contrasts as a proxy for elastic contrast.

In vertical strike-slip faults, small earthquakes generally propagate in two directions as a mixture of in-plane (mode II) and anti-plane (mode III) ruptures (e.g., Harris & Day, 2005). In contrast, for moderate and large strike-slip earthquakes (e.g., >M6.5), fault ruptures initiate with a mixture of mode II and III propagation, but after saturating the seismogenic zone, their subsequent propagation is predominantly lateral in mode II (e.g., Ben-Zion, 2006). Moreover, only mode II ruptures in strike-slip faults have been shown to exhibit the bimaterial coupling of shear slip and normal stress, generating the preferentially propagating wrinkle-like pulse (Ben-Zion & Andrews, 1998). The SCSZ is a vertical strike-slip fault which, based on the common occurrence of pseudotachylyte, experienced large earthquakes (Price et al., 2012; W. J. Song et al., 2020). Thus, in the present study, we consider 2D in-plane shear ruptures, horizontally propagating along the strike of the fault/shear zone and limit our discussion to wave velocities in the horizontal $x1$-$x2$ plane.

For a subshear rupture in bimaterial strike-slip faults, differential fault-normal particle motion near the rupture tip is key to the bimaterial coupling effect, and the contrast that governs the strength of the bimaterial effects is that of the *S*-wave velocities (Figures 1b and c; e.g., Ben-Zion, 2001; Ben-Zion & Andrews, 1998; Somerville et al., 1997). The fault-normal particle motion (parallel to the $x2$ axis) at the rupture tip for a subshear rupture is found only in the *SH* wave propagating parallel to the SCSZ-parallel slip direction at $\phi = 0^\circ$ (Figure S3b). We therefore disregard the *P* wave as well as the *SV* wave at $\phi = 0^\circ$ because its particle motion is parallel to the vertical fault/shear zone (Figure S3b).

The velocity contrast for the *SH* wave between the natural QF and schist rocks at $\phi = 0^\circ$ is 25.5%, and the schist is more compliant (Figures 4f). In Section 5.2, by analogy with the model of rupture dynamics for bimaterial faults in elastically isotropic media described above, we consider the *SH* wave as diagnostic in the SCSZ and discuss preferred rupture propagation in the slip direction of the more compliant schist and greater damage-zone width in the less compliant QF rock (Figures 1b and d). Below we deal with subshear and supershear rupture models assuming that the *SH* wave in our anisotropic rocks can substitute for the *S*-wave in isotropic rocks.

5.2. Comparison with previous isotropic bimaterial models

5.2.1. Subshear rupture model

In subshear rupture models of a bimaterial interface (fault) separating two elastically isotropic dissimilar materials, the presence of elastic contrast across the interface causes mismatch in seismic wave velocities and produces head waves that propagate along the fault and radiate to the more compliant medium (Ben-Zion, 1989, 1990). Thus, in addition to slower *P*- and *S*-wave fronts, two different head wave fronts (*P*-to-*P* between faster and slower *P* waves, and *S*-to-*S* between faster and slower *S* waves) propagate on the more compliant side (Figure 1b; e.g., Ben-Zion, 2001). Numerical results of Andrews and Ben-Zion (1997) and Ben-Zion and Andrews (1998) showed that the *S*-to-*S* head wave contributes to normal stress transition from compression during the buildup of the head wave to tension after arrival of the slower *S* wave, which allows pulse-like slip to occur at the rupture front. Therefore, wrinkle-like pulse ruptures are governed by the contrast of *S* wave velocities across the interface.

In those models, even though the up-down symmetry across the interface is lost, the *P*- and *S*-wave fronts remain circular in both stiff and compliant sides due to elastically isotropic media (Figure 1b). In contrast, seismic wave speed varies with propagation direction in anisotropic materials, resulting in non-spherical wave fronts. In addition, the shear wave in anisotropic media splits into two quasi-shear waves with different polarizations and velocities (e.g., qV_{SH} and qV_{SV}) and their polarizations are approximately orthogonal (e.g., Figure S3a), whereas no shear-wave splitting is observed in isotropic materials. Therefore, additional complexity arises in a bimaterial interface between anisotropic materials.

Figure 6 plots *P*-, *SH*- and *SV*-wave velocities in polar coordinates for the natural and synthetic rocks of the SCSZ, in which the QF rock is placed in the upper side (ϕ = 0° to 180°) and the schist in the lower side (ϕ = 180° to 360°). The lithologic contact or shear-zone core lies along the horizontal axis (ϕ = 0° or 180°), which is parallel to the fault/shear zone slip direction. Since the synthetic rocks have the same modal mineralogy and mica preferred orientation as the natural rocks, any differences in wave velocity patterns or wave fronts in Figure 6 between the synthetic and natural rocks are caused by other factors such as crystallographic orientations of quartz and plagioclase. Due to different degree of anisotropy in each rock, wave fronts in the QF and schist rocks show different variations, and therefore varying velocity contrasts are expected depending on propagation direction. For example, both natural and synthetic QF rocks with relatively weak anisotropy have sub-circular wave fronts, whereas both schists with strong anisotropy have non-circular wave fronts (Figure 6). In the schists, the *P* and *SV* waves are faster in the fault-parallel direction and slower in the fault-normal direction than those in the QF rocks (Figure 6). Since the *SH*-wave velocity pattern in the mica-rich schists with planar foliation is similar to single-crystal mica, their *SH* waves are slower than the QF rocks in all (for the synthetic rocks) or most (for the natural rocks) propagation directions including the fault-parallel and normal directions, indicating more compliant schists at most values of ϕ (Figures 4f, 5f and 6).

If we apply the numerical results of Andrews and Ben-Zion (1997) and Ben-Zion and Andrews (1998) in isotropic media to our velocity analysis, the contrast between *SH*-wave velocities across the SCSZ contact would govern the bimaterial effect that can lead to strongly asymmetric fault-normal particle motions and produce preferentially propagating wrinkle-like pulses. The *SV* wave with vertical polarization is not likely to facilitate bimaterial coupling and related effects. When considering a propagation direction parallel to the fault, at the rupture tip, rapid transition of normal stress and fault-normal motion from an *S*-to-*S* head wave to a slower *SH* wave of the schist would allow the pulse to propagate in the slip direction of the more compliant schist and hence to preferentially produce off-fault damage in the stiffer QF rock with the faster *SH* wave (Figure 6a). With repeated ruptures (e.g., Aben et al., 2016; Doan & d'Hour, 2012), we might expect a strongly asymmetric damage zone that is wider in the QF rocks, consistent with the asymmetric distribution of damage observed across the SCSZ (Figure 2d).

5.2.2. Supershear rupture model

Most ruptures propagate at velocities below the Rayleigh wave speed, or ~92% of the shear wave speed (Craggs, 1960; Freund, 1990), and as noted above, asymmetric rock damage around the SCSZ is consistent with material contrast across the shear zone and preferred propagation of subshear ruptures. However, theoretical and numerical studies (e.g., Andrews, 1976; Broberg, 1994, 1995; Burridge, 1973; Das and Aki, 1977; Freund, 1990; Gao et al., 2001; Liu et al., 2014; Shi et al., 2008) and laboratory experiments (e.g., Passelègue et al., 2013; Rosakis et al., 1999; Xia et al., 2004) demonstrate that rupture speed can exceed the shear wave speed and even reach the compressional wave speed. There is also growing evidence of these "supershear" earthquakes observed from large strike-slip faults in nature (e.g., Archuleta, 1984; Bouchon et al. 2001; Bouchon and Vallee 2003; Dunham and Archuleta, 2004; Socquet et al., 2019; Wang and Mori, 2012; Yue et al., 2013). In addition, experimental work suggests that subshear rupture might not produce high enough strain rates at sufficient distance to explain the width of pulverization around natural faults (e.g., Aben et al., 2017a; Griffith et al., 2018; Xu & Ben-Zion, 2017). For these reasons, supershear rupture has been considered as a possible mechanism for rock pulverization well off the main slip surface (Doan & Gary, 2009; Yuan et al., 2011) and such *S* shock waves are thought to have caused high strain rates at distance of up to several kilometers from the fault core (Bhat et al., 2007).

A supershear rupture along a bimaterial fault in elastically isotropic material preferentially propagates to the negative direction (e.g., Ranjith and Rice, 2001; Shlomai et al., 2020; Xia et al., 2005). Theoretical analysis of Ranjith and Rice (2001), for example, predicted that supershear ruptures with speeds close to a *P*-wave velocity of a more compliant material can propagate only in the negative direction. Xia et al. (2005) and Shlomai et al. (2020) experimentally observed supershear rupture along the negative direction at velocities approaching and exceeding the slower *P*-wave speed. Thus, if we assume a supershear rupture along the elastically anisotropic SCSZ and speculate that the *SH* wave with fault-parallel propagation is still important in determining material contrast and rupture directivity, then rupture would be more likely to propagate in the slip direction of the stiffer QF rocks, which is the opposite direction of preferred subshear rupture propagation. As a result, a wider damage zone would occur in the more compliant schist side, which is the opposite of what we observe in the SCSZ.

Alternatively, in numerical investigations, Shi and Ben-Zion (2006) observed supershear transitions in both directions along an isotropic bimaterial interface with velocities close to the *P*-wave speed of the more compliant material in the negative direction and close to the *P*-wave speed of the stiffer material in the positive direction. If this supershear rupture propagation produces off-fault damage, the resulting damage zones are likely to distribute symmetrically on both sides of the fault (Xu and Ben-Zion, 2017), which is inconsistent with our observation of asymmetric damage distribution. A possible explanation is that multiple bilateral supershear ruptures without a preferred-propagation direction have occurred, but that the asymmetric damage distribution may be caused by the different rock types (QF and schist) rather than rupture directivity. For example, Aben et al. (2017b) proposed that more compliant rocks on one side of the fault would respond differently to similar dynamic loading from stiffer rocks on the opposite side, leading to asymmetric damage. Their experimental results showed that layered anisotropic sandstone was not pulverized during dynamic loading. An open question regarding further experimental work is whether the strong anisotropy of the SCSZ schist might have a mitigating effect on damage, resulting in the asymmetric damage in the SCSZ. In addition, supershear ruptures along anisotropic bimaterial interfaces have not yet been explored numerically, so the relationship between supershear rupture directivity and damage distribution remains an open question.

5.3. Effect of mica content on seismic velocity contrast

The role of mica in seismic anisotropy has been relatively well studied because mica is recognized as a major contributor to observed seismic anisotropy in middle crustal settings owing to its high anisotropy and the common development of preferred shape and crystallographic orientation (e.g., Christensen, 1965; Dempsey et al., 2011; Kästner et al., 2021; Lloyd et al., 2009; Ward et al., 2012). However, we are not aware of studies that have explored the relationship between mica content and seismic velocity contrast, so here we employ synthetic microstructures to explore this relationship and compare our results to published velocity data from natural rocks with varying mica content.

5.3.1. Sensitivity analysis of varying mica content

To explore the role of mica content on seismic velocity contrast, we generate eleven synthetic microstructures with modal% mica ranging from 0% to 100% in 10% intervals using the technique described in Section 3.1 (Figures 7 and S7). In the synthetic microstructures, we use three types of relative proportions of biotite (Bt) and muscovite (Ms): (1) 100% biotite, (2) Bt:Ms = 50:50, and (3) 100% muscovite. The remaining mineralogy has 50:50 relative proportions of quartz and plagioclase in all the cases. As expected, the variations of 2D seismic velocities in the $x1$-$x2$ plane increase with increasing modal percentage of aligned mica (Figure 7b). Similarly, 3D seismic anisotropies of P and S waves (AV_{P} and AV_{SH} shown in Figure 7c) increase with mica modal percentage, which is consistent with previous work (e.g., Christensen, 1965; Dempsey et al., 2011; Kästner et al., 2021; Ward et al., 2012). We calculate velocity contrasts of these synthetic microstructures relative to the synthetic QF rock at ϕ = 0°. As $qV_{\mathrm{SH}}(0°)$ decreases with increasing mica content (Figure 7b), the contrast of $qV_{\mathrm{SH}}(0°)$ increases up to 33.9% for 100 modal% biotite (Figure 7d). The synthetic rocks with mica content greater than the synthetic QF rock (>14.1 modal%) are more compliant than the QF rock based on *SH*-wave velocity (Figure 7d). This might allow us to predict that if a rock has more content of preferentially oriented mica and higher anisotropy on one side of a mature bimaterial fault, then the rock is more compliant, the positive direction becomes the preferred rupture direction, and the fault would show asymmetric damage. This prediction may be valid given that rocks adjacent to large continental strike-slip faults such as the San Andreas fault generally have foliations oriented sub-parallel to the sub-vertical slip surface (e.g., Schulz and Evans, 2000).

5.3.2. Comparison with other natural rocks

To compare our sensitivity results with natural rocks, we used 133 rock samples from the literature for analysis of P-wave anisotropy (AV_P) and $qV_{SH}(0°)$ contrast in the direction parallel to the foliation and fault trace (see Table S2 for details). Felsic to intermediate rocks with varying mica content (igneous rocks, quartzite, mylonite, gneiss, and schist) are considered since they are commonly observed in the middle crust and have the same minerals as the SCSZ rocks, consisting of quartz, feldspars, biotite and muscovite as major components (>90 modal%). Figure 8a compares AV_P of our natural SCSZ QF and schist rocks with those from the literature, overlaid on the synthetic AV_P for reference. Of the literature data, seismic properties of 109 rock samples were obtained by petrophysical measurements up to 1 GPa confining pressure (Birch, 1960; Burke, 1991; Burke & Fountain, 1990; Burlini & Fountain, 1993; Chroston & Brooks, 1989; Cirrincione et al., 2010; Fountain et al., 1990; Godfrey et al., 2000; Hurich et al., 2001; Ji et al., 1997, 2015; Kästner et al., 2021; Kern et al., 1999, 2001, 2008, 2009; Khazanehdari et al., 2000; Long, 1994; Salisbury & Fountain, 1994). At room temperature, the velocity–pressure relations display a steep, non-linear increase of velocity with increasing confining pressure at low pressures (generally <100–300 MPa) due to progressive closure of microfractures, and then a gentle, nearly-linear increase of velocity with pressure at higher pressures related to intrinsic rock properties (e.g., Birch, 1960; Burlini & Fountain, 1993; Christensen, 1965; Kern et al., 2008, 2009; Kern & Wenk, 1990; Ji et al., 2015). The microfracture closure pressure (Pc), above which velocities increase linearly, is dependent on rock type and shape of pores and microfractures (e.g., Walsh, 1965). For taking intrinsic seismic properties of the rocks and comparison with EBSD analysis of the SCSZ samples and the other 24 rocks (Ji et al., 2015; Kästner et al., 2021; Lloyd et al., 2009; Naus-Thijssen, Goupee, Johnson, et al., 2011; Watling, 2017), we obtained the pressure derivative (dV/dP) and the velocity intercept V_0 at zero pressure by making and extrapolating a linear regression fit to the high-pressure part of each velocity–pressure curve above Pc (e.g., Almqvist & Mainprice, 2017; Burlini & Fountain, 1993; Ji et al., 2007; Kästner et al., 2021; Kern et al., 2001; Khazanehdari et al., 2000). This relationship in the linear regime is described by $V(P) = V_0 + (\mathrm{d}V/\mathrm{d}P)P$. The V_0 is used to calculate P-wave seismic anisotropies of the literature rock samples via the equation in Section 3.3. Generally, the 135 natural rock samples including the SCSZ rocks show increase in AV_P with increasing mica content (Figure 8a). However, most of them lie below the synthetic AV_P curve, presumably owing to microstructural differences from the synthetic microstructures, including (a) mica shape and crystallographic preferred orientation, (b) quartz and feldspar crystallographic preferred orientation, (c) minor accessory minerals, and (d) microfractures, pores and other defects that affect petrophysical measurements (Figure 8a). In addition, for the data obtained by EBSD analysis, AV_P can depend on single-crystal elastic properties and homogenization scheme used in computation of bulk stiffness. Of the 133 published data, 29 samples that have *S*-wave velocity data (V_0) and the information of rock-fabric orientation are used for the calculation of qV_{SH} contrast (Burlini & Fountain, 1993; Cirrincione et al., 2010; Godfrey et al., 2000; Ji et al., 2015; Kern et al., 2008, 2009; Naus-Thijssen, Goupee, Johnson, et al., 2011; Salisbury & Fountain, 1994). Figure 8b shows qV_{SH} contrast of 30 natural rock samples from the literature and the SCSZ schist relative to the natural SCSZ QF rock at ϕ = 0°, overlaid on the synthetic $qV_{SH}(0°)$ contrasts relative to the natural QF rock for reference. The rocks with greater mica content than the SCSZ QF rock show a general increase in $qV_{SH}(0°)$ contrast and are more compliant than the SCSZ QF rock, broadly consistent with the prediction from our synthetic rock analyses (Figure 8b). We note a positive correlation between seismic anisotropy (e.g., AV_P and AV_{SH}) and velocity contrast of $qV_{SH}(0°)$ in the direction parallel to the foliation or fault trace, and higher compliance with increasing modal% mica (Figures 7 and 8). These results suggest that regardless of rock type, the content of highly anisotropic minerals (e.g., mica) is an important factor in seismic anisotropy and seismic/elastic contrast that impacts the rupture directivity of strike-slip bimaterial faults.

5.4. Effects of preexisting damage and mylonitization on rupture propagation and asymmetric damage

The SCSZ core is surrounded by ~260-m-wide asymmetric effective damage zones composed of fractured rocks (Figure 2d). Damage zones in the upper crust appear seismically as a low-velocity zone with reduction in elastic stiffness relative to the intact host rocks (e.g., Cochran et al., 2009; Lewis & Ben-Zion, 2010; Li & Vernon, 2001). The damage zone observed in the SCSZ has evolved through multiple seismic cycles based on deformed pseudotachylyte and multiple sets of dynamic microfractures in minerals such as feldspars (Johnson, Song, Vel, et al., 2021; Price et al., 2012; B. R. Song et al., 2020). Therefore, accumulated microfractures produced during multiple earthquakes may potentially have caused significant reduction in stiffness of the more damaged QF rock, leading to changes in the material contrast across the shear zone. However, at middle crustal depths, healing/sealing processes in damaged rocks during post- and interseismic periods (e.g., Johnson, Song, Vel, et al., 2021) and closure of microfractures under high confining pressure may facilitate nearly complete recovery of elastic stiffness (e.g., Li et al., 2006). Thus, the long-term effect of damage on rupture dynamics in faults/shear zones at depth remains an open question.

In the present study, we used the SCSZ host rocks for elastic property measurements because we are interested in the early development and evolution of asymmetric damage. However, the rocks juxtaposed across the SCSZ are intensely deformed mylonite/ultramylonite and highly sheared schist. Such deformation can affect the intensity and pattern of seismic anisotropy and hence elastic contrast if it changes the strength of mica crystallographic preferred orientation, operates certain slip systems in minerals such as basal <a>, rhomb <a> or prism <a> slip in quartz (e.g., Ji et al., 2015; Mainprice & Casey, 1990; McDonough & Fountain, 1993; Ward et al., 2012), and develops structures such as S-C fabrics, crenulations and folds (e.g., Lloyd et al., 2009; Naus-Thijssen, Goupee, Johnson, et al., 2011). For example, during long-term tectonic deformation, mylonitization typically generates a strong macroscopic foliation, which may increase seismic anisotropy owing to transition to C-type fabric from S-C fabric during deformation (e.g., Kern & Wenk, 1990; Lloyd et al., 2009). On the other hand, mylonite with a strong foliation might have low seismic anisotropy compared to other rock types with the same mica content (e.g., Jones & Nur, 1982) if relatively strong crystallographic orientations of quartz and/or feldspar in mylonites mute seismic anisotropy generated by mica preferred orientation (e.g., Ward et al., 2012). In addition, the seismic properties of mylonites might be influenced by increase of fine grains and mixture of matrix phases during mylonitization and by change in deformation mechanism to grain-size-sensitive creep. Analysis of the SCSZ mylonite requires petrophysical techniques and is left for future work.

6. Conclusions

We calculated the bulk elastic properties and seismic wave velocities of two elastically anisotropic rocks (quartzofeldspathic rock and mica-rich schist) from either side of the SCSZ to investigate the effect of elastic contrast in anisotropic bimaterial strike-slip faults on preferentially propagating wrinkle-like pulse ruptures and asymmetric damage. Our results suggest that if micaceous foliation is well-developed parallel to a bimaterial fault in anisotropic rocks, for a pure mode II rupture along the fault, the elastic contrast most relevant to the rupture directivity and asymmetric damage is governed by the *SH* waves that propagate parallel to the fault with fault-normal polarization.

The damage zone across the SCSZ exhibits strongly asymmetric distribution with a much wider damage zone on the QF rock side in which the velocity of fault-parallel *SH* wave is higher. This damage asymmetry agrees with modeling predictions of a subshear rupture along an isotropic bimaterial interface (e.g., Ben-Zion and Shi, 2005; Xu & Ben-Zion, 2017) and field observations of bimaterial faults (e.g., Dor et al., 2008; Dor, Ben-Zion, et al., 2006; Dor, Rockwell, et al., 2006; Mitchell et al., 2011; Rempe et al., 2013) showing damage primarily on the side of the fault with higher seismic velocity. Thus, velocity contrast of the *SH* waves across bimaterial interfaces separating elastically anisotropic rocks appears to provide results that are consistent with numerical modeling results for bimaterial interfaces separating elastically isotropic rocks.

The intensity of contrast in *SH*-wave velocities between two rocks is strongly associated with orientation and proportion of preferentially aligned mica. Regardless of rock type, if a rock on one side of a bimaterial fault has a larger model% of mica with fault-parallel preferred orientation, then that rock is likely to have higher anisotropy and slower *SH* wave propagating parallel to the fault. Therefore, where mica constitutes an important modal% of the rocks, quantifying the influence of mica-induced seismic anisotropy on the elastic properties may be necessary for more precise determination of elastic contrasts and a better understanding of rupture directivity and asymmetric damage in elastically anisotropic bimaterial rupture.

Acknowledgments

This research was funded by National Science Foundation grants EAR-0820946, EAR-1347087 and EAR-1727090. B.R. Song was supported in part by a Michael J. Eckardt Dissertation Fellowship from the University of Maine. We thank Yehuda Ben-Zion for helpful discussion. Data used to produce Figure 2d are available in B. R. Song et al. (2020). All the other data including homogenized stiffness tensors of the natural and synthetic rocks used in the present study will be archived in a permanent repository (Figshare) prior to publication.

References

Aben, F. M., Doan, M.-L., Mitchell, T. M., Toussaint, R., Reuschlé, T., Fondriest, M., et al. (2016). Dynamic fracturing by successive coseismic loadings leads to pulverization in active fault zones. *Journal of Geophysical Research*, *121*(4), 2338–2360. https://doi.org/10.1002/2015JB012542

Aben, F. M., Doan, M.-L., Gratier, J.-P., & Renard, F. (2017a). Coseismic damage generation and pulverization in fault zones. In M. Y. Thomas, T. M. Mitchell, & H. S. Bhat (Eds.), *Fault Zone Dynamic Processes: Evolution of Fault Properties During Seismic Rupture, Geophysical Monograph Series* (Vol. 227, pp. 47–80). American Geophysical Union. https://doi.org/10.1002/9781119156895.ch4

Aben, F. M., Doan, M.-L., Gratier, J.-P., & Renard, F. (2017b). High strain rate deformation of porous sandstone and the asymmetry of earthquake damage in shallow fault zones. *Earth and Planetary Science Letters*, *463*, 81–91. https://doi.org/10.1016/j.epsl.2017.01.016

Adams, G. G. (1995). Self-Excited Oscillations of Two Elastic Half-Spaces Sliding With a Constant Coefficient of Friction. *Journal of Applied Mechanics*, *62*(4), 867–872. https://doi.org/10.1115/1.2896013

Adda-Bedia, M., & Ben Amar, M. (2003). Self-sustained slip pulses of finite size between dissimilar materials. *Journal of the Mechanics and Physics of Solids*, *51*(10), 1849–1861. https://doi.org/10.1016/S0022-5096(03)00068-1

Aleksandrov, K. S., & Ryzhova, T. V. (1961). Elastic properties of rock-forming minerals II: Layered silicates. *Bulletin of the Academy of Sciences of the U.S.S.R., Geophysics Series (English Translation)*, (12), 1165–1168.

Allam, A. A., Ben-Zion, Y., & Peng, Z. (2014). Seismic Imaging of a Bimaterial Interface Along the Hayward Fault, CA, with Fault Zone Head Waves and Direct P Arrivals. *Pure and Applied Geophysics*, *171*(11), 2993–3011. https://doi.org/10.1007/s00024-014-0784-0

Almqvist, B. S. G., & Mainprice, D. (2017). Seismic properties and anisotropy of the continental crust: Predictions based on mineral texture and rock microstructure. *Reviews of Geophysics*, *55*(2), 367–433. https://doi.org/10.1002/2016RG000552

Ampuero, J. P., & Ben-Zion, Y. (2008). Cracks, pulses and macroscopic asymmetry of dynamic rupture on a bimaterial interface with velocity-weakening friction. *Geophysical Journal International*, *173*(2), 674–692. https://doi.org/10.1111/j.1365-246X.2008.03736.x

Anderson, E. K., Song, W. J., Johnson, S. E., & Cruz-Uribe, A. M. (2021). Mica kink-band geometry as an indicator of coseismic dynamic loading. *Earth and Planetary Science Letters*, *567*, 117000. https://doi.org/10.1016/j.epsl.2021.117000

Andrews, D. J. (1976). Rupture Velocity of Plane Strain Shear Cracks. *Journal of Geophysical Research*, *81*(32), 5679–5687. https://doi.org/10.1029/JB081i032p05679

Andrews, D. J., & Ben-Zion, Y. (1997). Wrinkle-like slip pulse on a fault between different materials. *Journal of Geophysical Research*, *102*(B1), 553–571. https://doi.org/10.1029/96JB02856

Archuleta, R. J. (1984). A faulting model for the 1979 Imperial Valley earthquake. *Journal of Geophysical Research*, *89*(B6), 4559–4585. https://doi.org/10.1029/JB089iB06p04559

Audet, P. (2015). Layered crustal anisotropy around the San Andreas Fault near Parkfield, California. *Journal of Geophysical Research*, *120*(5), 3527–3543. https://doi.org/10.1002/2014JB011821

Auld, B. A. (1990). *Acoustic Fields and Waves in Solids, Volume 1* (2nd ed.). Malabar, FL: R. E. Krieger.

Babuška, V., & Cara, M. (1991). *Seismic Anisotropy in the Earth*. Dordrecht, Netherlands: Kluwer Academic Publishers. https://doi.org/10.1007/978-94-011-3600-6

Ben-Zion, Y. (1989). The response of two joined quarter spaces to SH line sources located at the material discontinuity interface. *Geophysical Journal International*, *98*(2), 213–222. https://doi.org/10.1111/j.1365-246X.1989.tb03346.x

Ben-Zion, Y. (1990). The response of two half spaces to point dislocations at the material interface. *Geophysical Journal International*, *101*(3), 507–528. https://doi.org/10.1111/j.1365-246X.1990.tb05567.x

Ben-Zion, Y. (2001). Dynamic ruptures in recent models of earthquake faults. *Journal of the Mechanics and Physics of Solids*, *49*(9), 2209–2244. https://doi.org/10.1016/S0022-5096(01)00036-9

Ben-Zion, Y. (2006). Comment on "The wrinkle-like slip pulse is not important in earthquake dynamics" by D. J. Andrews and R. A. Harris. *Geophysical Research Letters*, *33*(6), L06310 1-3. https://doi.org/10.1029/2005GL025372

Ben-Zion, Y., & Andrews, D. J. (1998). Properties and implications of dynamic rupture along a material interface. *Bulletin of the Seismological Society of America*, *88*(4), 1085–1094.

Ben-Zion, Y., & Huang, Y. (2002). Dynamic rupture on an interface between a compliant fault zone layer and a stiffer surrounding solid. *Journal of Geophysical Research*, *107*(B2), 2042. https://doi.org/10.1029/2001JB000254

Ben-Zion, Y., & Shi, Z. (2005). Dynamic rupture on a material interface with spontaneous generation of plastic strain in the bulk. *Earth and Planetary Science Letters*, *236*(1–2), 486–496. https://doi.org/10.1016/j.epsl.2005.03.025

Bernard, P., Herrero, A., & Berge, C. (1996). Modeling directivity of heterogeneous earthquake ruptures. *Bulletin of the Seismological Society of America*, *86*(4), 1149–1160.

Bertero, V. V., Mahin, S. A., & Herrera, R. A. (1978). Aseismic design implications of near-fault san fernando earthquake records. *Earthquake Engineering and Structural Dynamics Structural Dynamics*, *6*(1), 31–42. https://doi.org/10.1002/eqe.4290060105

Bhat, H. S., Dmowska, R., King, G. C. P., Klinger, Y., & Rice, J. R. (2007). Off-fault damage patterns due to supershear ruptures with application to the 2001 M_w 8.1 Kokoxili (Kunlun) Tibet earthquake. *Journal of Geophysical Research*, *112*(B6), B06301. https://doi.org/10.1029/2006JB004425

Birch, F. (1960). The velocity of compressional waves in rocks to 10 kilobars, part 1. *Journal of Geophysical Research*, *65*(4), 1083–1102. https://doi.org/10.1029/JZ065i004p01083

Boatwright, J., & Boore, D. M. (1982). Analysis of the ground accelerations radiated by the 1980 Livermore Valley earthquakes for directivity and dynamic source characteristics. *Bulletin of the Seismological Society of America*, *72*(6), 1843–1865. https://doi.org/10.1785/BSSA07206A1843

Bouchon, M., & Vallée, M. (2003). Observation of long supershear rupture during the magnitude 8.1 Kunlunshan earthquake. *Science*, *301*(5634), 824–826. https://doi.org/10.1126/science.1086832

Bouchon, M., Bouin, M. P., Karabulut, H., Toksöz, M. N., Dietrich, M., & Rosakis, A. J. (2001). How fast is rupture during an earthquake? New insights from the 1999 Turkey earthquakes. *Geophysical Research Letters*, *28*(14), 2723–2726. https://doi.org/10.1029/2001GL013112

Bray, J. D., Rodriguez-Marek, A., & Gillie, J. L. (2009). Design ground motions near active faults. *Bulletin of the New Zealand Society for Earthquake Engineering*, *42*(1), 1–8. https://doi.org/10.5459/bnzsee.42.1.1-8

Brener, E. A., Weikamp, M., Spatschek, R., Bar-Sinai, Y., & Bouchbinder, E. (2016). Dynamic instabilities of frictional sliding at a bimaterial interface. *Journal of the Mechanics and Physics of Solids*, *89*, 149–173. https://doi.org/10.1016/j.jmps.2016.01.009

Brietzke, G. B., Cochard, A., & Igel, H. (2007). Dynamic rupture along bimaterial interfaces in 3D. *Geophysical Research Letters*, *34*(11), L11305 1-5. https://doi.org/10.1029/2007GL029908

Brietzke, G. B., Cochard, A., & Igel, H. (2009). Importance of bimaterial interfaces for earthquake dynamics and strong ground motion. *Geophysical Journal International*, *178*(2), 921–938. https://doi.org/10.1111/j.1365-246X.2009.04209.x

Broberg, K. B. (1994). Intersonic Bilateral Slip. *Geophysical Journal International*, *119*(3), 706–714. https://doi.org/10.1111/j.1365-246X.1994.tb04010.x

Broberg, K. B. (1995). Intersonic mode II crack expansion. *Archives of Mechanics*, *47*(5), 859–871.

Brown, J. M., Angel, R. J., & Ross, N. L. (2016). Elasticity of plagioclase fledpsars. *Journal of Geophysical Research*, *121*(2), 663–675. https://doi.org/10.1002/2015JB012736

Burke, M. M. (1991). *Reflectivity of Highly Deformed Terranes Based on Laboratory and In Situ Velocity Measurements from the Grenville Front Tectonic Zone, Central Ontario, Canada* (Doctoral dissertation). Retrieved from http://hdl.handle.net/10222/55211. Halifax, NS, Canada: Dalhousie University.

Burke, M. M., & Fountain, D. M. (1990). Seismic properties of rocks from an exposure of extended continental crust—new laboratory measurements from the Ivrea Zone. *Tectonophysics*, *182*(1–2), 119–146. https://doi.org/10.1016/0040-1951(90)90346-A

Burlini, L., & Fountain, D. M. (1993). Seismic anisotropy of metapelites from the Ivrea-Verbano zone and Serie dei Laghi (northern Italy). *Physics of the Earth and Planetary Interiors*, *78*(3), 301–317. https://doi.org/10.1016/0031-9201(93)90162-3

Burridge, R. (1973). Admissible Speeds for Plane-Strain Self-Similar Shear Cracks with Friction but Lacking Cohesion. *Geophysical Journal of the Royal Astronomical Society*, *35*(4), 439–455. https://doi.org/10.1111/j.1365-246X.1973.tb00608.x

Champion, C., & Liel, A. (2012). The effect of near-fault directivity on building seismic collapse risk. *Earthquake Engineering and Structural Dynamics*, *41*(10), 1391–1409. https://doi.org/10.1002/eqe.1188

Chheda, T. D., Mookherjee, M., Mainprice, D., dos Santos, A. M., Molaison, J. J., Chantel, J., et al. (2014). Structure and elasticity of phlogopite under compression: Geophysical implications. *Physics of the Earth and Planetary Interiors*, *233*, 1–12. https://doi.org/10.1016/j.pepi.2014.05.004

Christensen, N. I. (1965). Compressional wave velocities in metamorphic rocks at pressures to 10 kilobars. *Journal of Geophysical Research*, *70*(24), 6147–6164. https://doi.org/10.1029/JZ070I024P06147

Christensen, N. I., & Mooney, W. D. (1995). Seismic velocity structure and composition of the continental crust: A global view. *Journal of Geophysical Research*, *100*(B6), 9761–9788. https://doi.org/10.1029/95JB00259

Christensen, N. I., & Okaya, D. A. (2007). Compressional and shear wave velocities in south island, New Zealand rocks and their application to the interpretation of seismological models of the New Zealand crust. In D. Okaya, T. Stern, & F. Davey (Eds.), *A Continental Plate Boundary: Tectonics at South Island, New Zealand* (Vol. 175, pp. 123–155). https://doi.org/10.1029/175GM08

Christoffel, E. B. (1877). Ueber die Fortpflanzung von Stössen durch elastische feste Körper. *Annali Di Matematica Pura Ed Applicata*, *8*, 193–243. https://doi.org/10.1007/bf02420789

Chroston, P. N., & Brooks, S. G. (1989). Lower crustal seismic velocities from Lofoten-Vesterålen, North Norway. *Tectonophysics*, *157*(4), 251–269. https://doi.org/10.1016/0040-1951(89)90143-1

Cirrincione, R., Fazio, E., Heilbronner, R., Kern, H., Mengel, K., Ortolano, G., et al. (2010). Microstructure and elastic anisotropy of naturally deformed leucogneiss from a shear zone in Montalto (southern Calabria, Italy). *Geological Society, London, Special Publications*, *332*, 49–68. https://doi.org/10.1144/SP332.4

Cochard, A., & Rice, J. R. (2000). Fault rupture between dissimilar materials: Ill-posedness, regularization, and slip-pulse response. *Journal of Geophysical Research*, *105*(B11), 25891–25907. https://doi.org/10.1029/2000jb900230

Cochran, E. S., Li, Y.-G., Shearer, P. M., Barbot, S., Fialko, Y., & Vidale, J. E. (2009). Seismic and geodetic evidence for extensive, long-lived fault damage zones. *Geology*, *37*(4), 315–318. https://doi.org/10.1130/G25306A.1

Cook, A. C., Vel, S. S., Johnson, S. E., Gerbi, C. C., & Song, W. J. (2018). ThermoElastic and Seismic Analysis (TESA) toolbox for polycrystalline materials. Retrieved from https://umaine.edu/mecheng/vel/software/tesa_toolbox/

Craggs, J. W. (1960). On the propagation of a crack in an elastic-brittle material. *Journal of the Mechanics and Physics of Solids*, *8*(1), 66–75. https://doi.org/10.1016/0022-5096(60)90006-5

Cyprych, D., Piazolo, S., & Almqvist, B. S. G. (2017). Seismic anisotropy from compositional banding in granulites from the deep magmatic arc of Fiordland, New Zealand. *Earth and Planetary Science Letters*, *477*, 156–167. https://doi.org/10.1016/j.epsl.2017.08.017

Dalguer, L. A., & Day, S. M. (2009). Asymmetric rupture of large aspect-ratio faults at bimaterial interface in 3D. *Geophysical Research Letters*, *36*(23), 1–5. https://doi.org/10.1029/2009GL040303

Dalguer, L. A., Irikura, K., & Riera, J. D. (2003). Simulation of tensile crack generation by three-dimensional dynamic shear rupture propagation during an earthquake. *Journal of Geophysical Research*, *108*(B3), ESE 3-1-ESE 3-20. https://doi.org/10.1029/2001jb001738

Danesi, S., Bannister, S., & Morelli, A. (2007). Repeating earthquakes from rupture of an asperity under an Antarctic outlet glacier. *Earth and Planetary Science Letters*, *253*(1–2), 151–158. https://doi.org/10.1016/j.epsl.2006.10.023

Das, S., & Aki, K. (1977). A numerical study of two-dimensional spontaneous rupture propagation. *Geophysical Journal of the Royal Astronomical Society*, *50*(3), 643–668. https://doi.org/10.1111/j.1365-246X.1977.tb01339.x

Dempsey, E. D., Prior, D. J., Mariani, E., Toy, V. G., & Tatham, D. J. (2011). Mica-controlled anisotropy within mid-to-upper crustal mylonites: an EBSD study of mica fabrics in the Alpine Fault Zone, New Zealand. *Geological Society, London, Special Publications*, *360*, 33–47. https://doi.org/10.1144/SP360.3

Doan, M.-L., & d'Hour, V. (2012). Effect of initial damage on rock pulverization along faults. *Journal of Structural Geology*, *45*, 113–124. https://doi.org/10.1016/j.jsg.2012.05.006

Doan, M.-L., & Gary, G. (2009). Rock pulverization at high strain rate near the San Andreas fault. *Nature Geoscience*, *2*(10), 709–712. https://doi.org/10.1038/ngeo640

Doll, W. E., Domoracki, W. J., Costain, J. K., Çoruh, C., Ludman, A., & Hopeck, J. T. (1996). Seismic reflection evidence for the evolution of a transcurrent fault system: The Norumbega fault zone, Maine. *Geology*, *24*(3), 251–254. https://doi.org/10.1130/0091-7613(1996)024<0251:SREFTE>2.3.CO;2

Dor, O., Rockwell, T. K., & Ben-Zion, Y. (2006). Geological observations of damage asymmetry in the structure of the San Jacinto, San Andreas and Punchbowl faults in Southern California: A possible indicator for preferred rupture propagation direction. *Pure and Applied Geophysics*, *163*(2–3), 301–349. https://doi.org/10.1007/s00024-005-0023-9

Dor, O., Ben-Zion, Y., Rockwell, T. K., & Brune, J. (2006). Pulverized rocks in the Mojave section of the San Andreas Fault Zone. *Earth and Planetary Science Letters*, *245*(3–4), 642–654. https://doi.org/10.1016/j.epsl.2006.03.034

Dor, O., Yildirim, C., Rockwell, T. K., Ben-Zion, Y., Emre, O., Sisk, M., & Duman, T. Y. (2008). Geological and geomorphologic asymmetry across the rupture zones of the 1943 and 1944 earthquakes on the North Anatolian Fault: Possible signals for preferred earthquake propagation direction. *Geophysical Journal International*, *173*(2), 483–504. https://doi.org/10.1111/j.1365-246X.2008.03709.x

Dunham, E. M., & Archuleta, R. J. (2004). Evidence for a supershear transient during the 2002 Denali fault earthquake. *Bulletin of the Seismological Society of America*, *94*(6B), S256–S268. https://doi.org/10.1785/0120040616

Erickson, B. A., & Day, S. M. (2016). Bimaterial effects in an earthquake cycle model using rate-and-state friction. *Journal of Geophysical Research*, *121*(4), 2480–2506. https://doi.org/10.1002/2015JB012470

Fountain, D. M., Salisbury, M. H., & Percival, J. (1990). Seismic structure of the continental crust based on rock velocity measurements from the Kapuskasing Uplift. *Journal of Geophysical Research*, *95*(B2), 1167–1186. https://doi.org/10.1029/JB095iB02p01167

Freund, L. B. (1990). *Dynamic Fracture Mechanics*. Cambridge University Press. https://doi.org/10.1017/CBO9780511546761

Gao, H., Huang, Y., & Abraham, F. F. (2001). Continuum and atomistic studies of intersonic crack propagation. *Journal of the Mechanics and Physics of Solids*, *49*(9), 2113–2132. https://doi.org/10.1016/S0022-5096(01)00032-1

Godfrey, N. J., Christensen, N. I., & Okaya, D. A. (2000). Anisotropy of schists: Contribution of crustal anisotropy to active source seismic experiments and shear wave splitting observations. *Journal of Geophysical Research*, *105*(B12), 27991–28007. https://doi.org/10.1029/2000JB900286

Goldstein, A., & Hepburn, J. C. (1999). Possible correlations of the Norumbega fault system with faults in southeastern New England. In A. Ludman & D. P. West Jr. (Eds.), *Norumbega Fault System of the Northern Appalachians. Geological Society of American Special Paper Vol. 331* (pp. 73–83). Boulder, CO: Geological Society of America. https://doi.org/10.1130/0-8137-2331-0.73

Griffith, W. A., Rosakis, A., Pollard, D. D., & Ko, C. W. (2009). Dynamic rupture experiments elucidate tensile crack development during propagating earthquake ruptures. *Geology*, *37*(9), 795–798. https://doi.org/10.1130/G30064A.1

Griffith, W. A., St. Julien, R. C., Ghaffari, H. O., & Barber, T. J. (2018). A tensile origin for fault rock pulverization. *Journal of Geophysical Research*, *123*(8), 7055–7073. https://doi.org/10.1029/2018JB015786

Grover, T. W., & Fernandes, L. C. (2003). Bedrock geology of the Weeks Mills Quadrangle, Maine. *Maine Geological Survey, Open-File Map 03-49*, color map, scale 1:24000. Retrieved from https://digitalmaine.com/mgs_maps/31/

Hall, J. F., Heaton, T. H., Halling, M. W., & Wald, D. J. (1995). Near-Source Ground Motion and its Effects on Flexible Buildings. *Earthquake Spectra*, *11*(4), 569–605. https://doi.org/10.1193/1.1585828

Handy, M. R., Hirth, G., & Bürgmann, R. (2007). Continental fault ftructure and rheology from the frictional-to-viscous transition downward. In M. R. Handy, G. Hirth, & N. Hovius (Eds.), *Tectonic Faults: Agents of Change on a Dynamic Earth* (pp. 139–182). The MIT Press. https://doi.org/10.7551/mitpress/6703.003.0008

Harris, R. A., & Day, S. M. (1997). Effects of a low-velocity zone on a dynamic rupture. *Bulletin of the Seismological Society of America*, *87*(5), 1267–1280. https://doi.org/10.1785/BSSA0870051267

Harris, R. A., & Day, S. M. (2005). Material contrast does not predict earthquake rupture propagation direction. *Geophysical Research Letters*, *32*(23), L23301 1-4. https://doi.org/10.1029/2005GL023941

Hubbard, M. S. (1999). Norumbega fault zone: Part of an orogen-parallel strike-slip system, northern Appalachians. In A. Ludman & D. P. West Jr. (Eds.), *Norumbega Fault System of the Northern Appalachians* (pp. 155–165). Geological Society of America Special Paper 331. https://doi.org/10.1130/0-8137-2331-0.155

Hurich, C. A., Deemer, S. J., Indares, A., & Salisbury, M. (2001). Compositional and metamorphic controls on velocity and reflectivity in the continental crust: An example from the Grenville Province of eastern Québec. *Journal of Geophysical Research*, *106*(B1), 665–682. https://doi.org/10.1029/2000JB900244

Hussey, A. M. (1988). Lithotectonic stratigraphy, deformation, plutonism, and metamorphism, greater Casco Bay region, southwestern Maine. In R. D. Tucker & R. G. Marvinney (Eds.), *Studies in Maine geology: Volume 1 - Structure and stratigraphy* (Vol. 1, pp. 17–34). Maine Geological Survey.

Hussey, A. M., Bothner, W. A., & Thomson, J. A. (1986). Geological comparisons across the Norumbega fault zone, southwestern Maine. In D. W. Newburg (Ed.), *New England Intercollegiate Geological Conference: Guidebook for Field Trips in Southwestern Maine* (pp. 53–78).

Jefferies, S. P., Holdsworth, R. E., Wibberley, C. A. J., Shimamoto, T., Spiers, C. J., Niemeijer, A. R., & Lloyd, G. E. (2006). The nature and importance of phyllonite development in crustal-scale fault cores: an example from the Median Tectonic Line, Japan. *Journal of Structural Geology*, *28*(2), 220–235. https://doi.org/10.1016/j.jsg.2005.10.008

Ji, S., Long, C., Martignole, J., & Salisbury, M. (1997). Seismic reflectivity of a finely layered, granulite-facies ductile shear zone in the southern Grenville Province (Quebec). *Tectonophysics*, *279*(1–4), 113–133. https://doi.org/10.1016/S0040-1951(97)00133-9

Ji, S., Wang, Q., Marcotte, D., Salisbury, M. H., & Xu, Z. (2007). P wave velocities, anisotropy and hysteresis in ultrahigh-pressure metamorphic rocks as a function of confining pressure. *Journal of Geophysical Research*, *112*(B9), B09204. https://doi.org/10.1029/2006JB004867

Ji, S., Shao, T., Michibayashi, K., Oya, S., Satsukawa, T., Wang, Q., et al. (2015). Magnitude and symmetry of seismic anisotropy in mica- and amphibole-bearing metamorphic rocks and implications for tectonic interpretation of seismic data from the southeast Tibetan Plateau. *Journal of Geophysical Research*, *120*(9), 6404–6430. https://doi.org/10.1002/2015JB012209

Johnson, S. E., Lenferink, H. J., Price, N. A., Marsh, J. H., Koons, P. O., West, D. P., Jr., & Beane, R. (2009). Clast-based kinematic vorticity gauges: The effects of slip at matrix/clast interfaces. *Journal of Structural Geology*, *31*(11), 1322–1339. https://doi.org/10.1016/j.jsg.2009.07.008

Johnson, S. E., Song, W. J., Vel, S. S., Song, B. R., & Gerbi, C. C. (2021). Energy partitioning, dynamic fragmentation, and off-fault damage in the earthquake source volume. *Journal of Geophysical Research*. https://doi.org/10.1029/2021JB022616

Johnson, S. E., Song, W. J., Cook, A. C., Vel, S. S., & Gerbi, C. C. (2021). The quartz α↔β phase transition: Does it drive damage and reaction in continental crust? *Earth and Planetary Science Letters*, *553*, 116622. https://doi.org/10.1016/j.epsl.2020.116622

Jones, T., & Nur, A. (1982). Seismic velocity and anisotropy in mylonites and the reflectivity of deep crustal fault zones. *Geology*, *10*(5), 260–263. https://doi.org/10.1130/0091-7613(1982)10<260:SVAAIM>2.0.CO;2

Kalkan, E., & Kunnath, S. K. (2006). Effects of fling step and forward directivity on seismic response of buildings. *Earthquake Spectra*, *22*(2), 367–390. https://doi.org/10.1193/1.2192560

Kästner, F., Pierdominici, S., Zappone, A., Morales, L. F. G., Schleicher, A. M., Wilke, F. D. H., & Berndt, C. (2021). Cross-scale seismic anisotropy analysis in metamorphic rocks from the COSC-1 borehole in the Scandinavian Caledonides. *Journal of Geophysical Research:*, *126*(5), e2020JB021154. https://doi.org/10.1029/2020JB021154

Kern, H., & Wenk, H.-R. (1990). Fabric-related velocity anisotropy and shear wave splitting in rocks from the Santa Rosa Mylonite Zone, California. *Journal of Geophysical Research*, *95*(B7), 11213–11223. https://doi.org/10.1029/JB095iB07p11213

Kern, H., Gao, S., Jin, Z., Popp, T., & Jin, S. (1999). Petrophysical studies on rocks from the Dabie ultrahigh-pressure (UHP) metamorphic belt, Central China: implications for the composition and delamination of the lower crust. *Tectonophysics*, *301*(3–4), 191–215. https://doi.org/10.1016/S0040-1951(98)00268-6

Kern, H., Popp, T., Gorbatsevich, F., Zharikov, A., Lobanov, K. V, & Smirnov, Y. . (2001). Pressure and temperature dependence of V_P and V_S in rocks from the superdeep well and from surface analogues at Kola and the nature of velocity anisotropy. *Tectonophysics*, *338*(2), 113–134. https://doi.org/10.1016/S0040-1951(01)00128-7

Kern, H., Ivankina, T. I., Nikitin, A. N., Lokajíček, T., & Pros, Z. (2008). The effect of oriented microcracks and crystallographic and shape preferred orientation on bulk elastic anisotropy of a foliated biotite gneiss from Outokumpu. *Tectonophysics*, *457*(3–4), 143–149. https://doi.org/10.1016/j.tecto.2008.06.015

Kern, H., Mengel, K., Strauss, K. W., Ivankina, T. I., Nikitin, A. N., & Kukkonen, I. T. (2009).

Elastic wave velocities, chemistry and modal mineralogy of crustal rocks sampled by the Outokumpu scientific drill hole: Evidence from lab measurements and modeling. *Physics of the Earth and Planetary Interiors*, *175*(3–4), 151–166. https://doi.org/10.1016/j.pepi.2009.03.009

Khazanehdari, J., Rutter, E. H., & Brodie, K. H. (2000). High-pressure-high-temperature seismic velocity structure of the midcrustal and lower crustal rocks of the Ivrea-Verbano zone and Serie dei Laghi, NW Italy. *Journal of Geophysical Research*, *105*(B6), 13843–13858. https://doi.org/10.1029/2000JB900025

Langer, S., Olsen-Kettle, L., & Weatherley, D. (2012). Identification of supershear transition mechanisms due to material contrast at bimaterial faults. *Geophysical Journal International*, *190*(2), 1169–1180. https://doi.org/10.1111/j.1365-246X.2012.05535.x

Lewis, M. A., & Ben-Zion, Y. (2010). Diversity of fault zone damage and trapping structures in the Parkfield section of the San Andreas Fault from comprehensive analysis of near fault seismograms. *Geophysical Journal International*, *183*(3), 1579–1595. https://doi.org/10.1111/j.1365-246X.2010.04816.x

Li, Y.-G., & Vernon, F. L. (2001). Characterization of the San Jacinto fault zone near Anza, California, by fault zone trapped waves. *Journal of Geophysical Research*, *106*(B12), 30671–30688. https://doi.org/10.1029/2000JB000107

Li, Y.-G., Chen, P., Cochran, E. S., Vidale, J. E., & Burdette, T. (2006). Seismic evidence for rock damage and healing on the San Andreas fault associated with the 2004 M 6.0 Parkfield earthquake. *Bulletin of the Seismological Society of America*, *96*(4B), S349–S363. https://doi.org/10.1785/0120050803

Li, Z., Zhang, H., & Peng, Z. (2014). Structure-controlled seismic anisotropy along the Karadere-Düzce branch of the North Anatolian Fault revealed by shear-wave splitting tomography. *Earth and Planetary Science Letters*, *391*, 319–326. https://doi.org/10.1016/j.epsl.2014.01.046

Liu, C., Bizzarri, A., & Das, S. (2014). Progression of spontaneous in-plane shear faults from sub-Rayleigh to compressional wave rupture speeds. *Journal of Geophysical Research*, *119*(11), 8331–8345. https://doi.org/10.1002/2014JB011187

Lloyd, G. E., Butler, R. W. H., Casey, M., & Mainprice, D. (2009). Mica, deformation fabrics and the seismic properties of the continental crust. *Earth and Planetary Science Letters*, *288*(1–2), 320–328. https://doi.org/10.1016/j.epsl.2009.09.035

Long, C. (1994). *Seismic Nature of Middle Continental Crust: Comparison of Laboratory Velocity and LITHOPROBE Seismic Reflection and Refraction Data from the Britt Domain, Southwestern Grenville Province, Canada* (Doctoral dissertation). Retrieved from http://hdl.handle.net/10222/55018. Halifax, NS, Canada: Dalhousie University.

Long, C., & Salisbury, M. H. (1996). The velocity structure of the Britt Domain, southwestern Grenville Province, from laboratory and refraction experiments. *Canadian Journal of Earth Sciences*, *33*(5), 729–745. https://doi.org/10.1139/e96-056

Ludman, A. (1998). Evolution of a transcurrent fault system in shallow crustal metasedimentary rocks: The Norumbega fault zone, eastern Maine. *Journal of Structural Geology*, *20*(1), 93–107. https://doi.org/10.1016/S0191-8141(97)00094-1

Ludman, A., Lanzirotti, A., Lux, D., & Wang, C. (1999). Constraints on timing and displacement of multistage shearing in the Norumbega fault system, eastern Maine. In A. Ludman & D. P. West Jr. (Eds.), *Norumbega Fault System of the Northern Appalachians. Geological Society of American Special Paper Vol. 331* (pp. 179–194). Boulder, CO: Geological Society of America. https://doi.org/10.1130/0-8137-2331-0.179

Mainprice, D., & Casey, M. (1990). The calculated seismic properties of quartz mylonites with typical fabrics: relationship to kinematics and temperature. *Geophysical Journal International*, *103*(3), 599–608. https://doi.org/10.1111/J.1365-246X.1990.TB05674.X

McDonough, D. T., & Fountain, D. M. (1993). P-wave anisotropy of mylonitic and infrastructural rocks from a Cordilleran core complex: the Ruby-East Humboldt Range, Nevada. *Physics of the Earth and Planetary Interiors*, *78*(3–4), 319–336. https://doi.org/10.1016/0031-9201(93)90163-4

Mitchell, T. M., Ben-Zion, Y., & Shimamoto, T. (2011). Pulverized fault rocks and damage asymmetry along the Arima-Takatsuki Tectonic Line, Japan. *Earth and Planetary Science Letters, 308*(3–4), 284–297. https://doi.org/10.1016/j.epsl.2011.04.023

Naus-Thijssen, F. M. J., Goupee, A. J., Johnson, S. E., Vel, S. S., & Gerbi, C. (2011). The influence of crenulation cleavage development on the bulk elastic and seismic properties of phyllosilicate-rich rocks. *Earth and Planetary Science Letters, 311*(3–4), 212–224. https://doi.org/10.1016/j.epsl.2011.08.048

Naus-Thijssen, F. M. J., Goupee, A. J., Vel, S. S., & Johnson, S. E. (2011). The influence of microstructure on seismic wave speed anisotropy in the crust: Computational analysis of quartz-muscovite rocks. *Geophysical Journal International*, *185*(2), 609–621. https://doi.org/10.1111/j.1365-246X.2011.04978.x

Newberg, D. W. (1985). Bedrock Geology of the Palermo 7.5' Quadrangle, Maine. *Maine Geological Survey, Open-File Map 85-84*, 14 page report and map, scale 1:24000.

Ohno, I., Harada, K., & Yoshitomi, C. (2006). Temperature variation of elastic constants of quartz across the α - β transition. *Physics and Chemistry of Minerals*, *33*(1), 1–9. https://doi.org/10.1007/s00269-005-0008-3

Okubo, K., Bhat, H. S., Rougier, E., Marty, S., Schubnel, A., Lei, Z., et al. (2019). Dynamics, radiation, and overall energy budget of earthquake rupture with coseismic off-fault damage. *Journal of Geophysical Research*, *124*(11), 11771–11801. https://doi.org/10.1029/2019JB017304

Pankiwskyj, K. (1996). Structure and stratigraphy across the Hackmatack Pond Fault, Kennebec and Waldo Counties, Maine. *Maine Geological Survey, Open-File Map 96-2*, 15 page report and 2 maps, scale 1:24000.

Passelègue, F. X., Schubnel, A., Nielsen, S., Bhat, H. S., & Madariaga, R. (2013). From sub-Rayleigh to supershear ruptures during stick-slip experiments on crustal rocks. *Science*, *340*(6137), 1208–1211. https://doi.org/10.1126/science.1235637

Prando, F., Menegon, L., Anderson, M., Marchesini, B., Mattila, J., & Viola, G. (2020). Fluid-mediated, brittle-ductile deformation at seismogenic depth - Part 2: Stress history and fluid pressure variations in a shear zone in a nuclear waste repository (Olkiluoto Island, Finland). *Solid Earth*, *11*(2), 489–511. https://doi.org/10.5194/se-11-489-2020

Price, N. A., Johnson, S. E., Gerbi, C. C., & West, D. P., Jr. (2012). Identifying deformed pseudotachylyte and its influence on the strength and evolution of a crustal shear zone at the base of the seismogenic zone. *Tectonophysics*, *518–521*, 63–83. https://doi.org/10.1016/j.tecto.2011.11.011

Price, N. A., Song, W. J., Johnson, S. E., Gerbi, C. C., Beane, R. J., & West, D. P., Jr. (2016). Recrystallization fabrics of sheared quartz veins with a strong pre-existing crystallographic preferred orientation from a seismogenic shear zone. *Tectonophysics*, *682*, 214–236. https://doi.org/10.1016/j.tecto.2016.05.030

Ranjith, K., & Rice, J. R. (2001). Slip dynamics at an interface between dissimilar materials.

Journal of the Mechanics and Physics of Solids, *49*(2), 341–361. https://doi.org/10.1016/S0022-5096(00)00029-6

Rempe, M., Mitchell, T., Renner, J., Nippress, S., Ben-Zion, Y., & Rockwell, T. (2013). Damage and seismic velocity structure of pulverized rocks near the San Andreas Fault. *Journal of Geophysical Research*, *118*(6), 2813–2831. https://doi.org/10.1002/jgrb.50184

Rice, J. R., Lapusta, N., & Ranjith, K. (2001). Rate and state dependent friction and the stability of sliding between elastically deformable solids. *Journal of the Mechanics and Physics of Solids*, *49*(9), 1865–1898. https://doi.org/10.1016/S0022-5096(01)00042-4

Rosakis, A. J., Samudrala, O., & Coker, D. (1999). Cracks Faster Than the Shear Wave Speed, *284*(5418), 1337–1340. https://doi.org/10.1126/science.284.5418.1337

Salisbury, M. H., & Fountain, D. M. (1994). The seismic velocity and Poisson's ratio structure of the Kapuskasing uplift from laboratory measurements. *Canadian Journal of Earth Sciences*, *31*(7), 1052–1063. https://doi.org/10.1139/e94-095

Shi, Z., & Ben-Zion, Y. (2006). Dynamic rupture on a bimaterial interface governed by slip-weakening friction. *Geophysical Journal International*, *165*(2), 469–484. https://doi.org/10.1111/j.1365-246X.2006.02853.x

Shi, Z., Ben-Zion, Y., & Needleman, A. (2008). Properties of dynamic rupture and energy partition in a solid with a frictional interface. *Journal of the Mechanics and Physics of Solids*, *56*(1), 5–24. https://doi.org/10.1016/j.jmps.2007.04.006

Shlomai, H., Adda-Bedia, M., Arias, R. E., & Fineberg, J. (2020). Supershear Frictional Ruptures Along Bimaterial Interfaces. *Journal of Geophysical Research*, *125*(8), 1–19. https://doi.org/10.1029/2020JB019829

Socquet, A., Hollingsworth, J., Pathier, E., & Bouchon, M. (2019). Evidence of supershear during the 2018 magnitude 7.5 Palu earthquake from space geodesy. *Nature Geoscience*, *12*(3), 192–199. https://doi.org/10.1038/s41561-018-0296-0

Somerville, P. G., Smith, N. F., Graves, R. W., & Abrahamson, N. A. (1997). Modification of empirical strong ground motion attenuation relations to include the amplitude and duration effects of rupture directivity. *Seismological Research Letters*, *68*(1), 199–222. https://doi.org/10.1785/gssrl.68.1.199

Song, B. R., Johnson, S. E., Song, W. J., Gerbi, C. C., & Yates, M. G. (2020). Coseismic damage runs deep in continental strike-slip faults. *Earth and Planetary Science Letters*, *539*, 116226.

https://doi.org/10.1016/j.epsl.2020.116226

Song, W. J., Johnson, S. E., & Gerbi, C. C. (2020). Quartz fluid inclusion abundance and off-fault damage in a deeply exhumed, strike-slip, seismogenic fault. *Journal of Structural Geology*, *139*, 104118. https://doi.org/10.1016/j.jsg.2020.104118

Swanson, M. T. (1992). Late Acadian-Alleghenian transpressional deformation: evidence from asymmetric boudinage in the Casco Bay Area, coastal Maine. *Journal of Structural Geology*, *14*(3), 323–341. https://doi.org/10.1016/0191-8141(92)90090-J

Swanson, M. T., Pollock, S. G., & Hussey, A. M. (1986). The structural and stratigraphic development of the Casco Bay Group at Harpswell Neck, Maine. In *New England Intercollegiate Geological Conference: Guidebook for Field Trips in Southwestern Maine* (pp. 350–370).

Thomas, M. Y., & Bhat, H. S. (2018). Dynamic evolution of off-fault medium during an earthquake: A micromechanics based model. *Geophysical Journal International*, *214*(2), 1267–1280. https://doi.org/10.1093/gji/ggy129

Thomas, M. Y., Bhat, H. S., & Klinger, Y. (2017). Effect of brittle off-fault damage on earthquake rupture dynamics. In M. Y. Thomas, T. M. Mitchell, & H. S. Bhat (Eds.), *Fault Zone Dynamic Processes: Evolution of Fault Properties During Seismic Rupture* (pp. 225–280). American Geophysical Union Geophysical Monograph 227. https://doi.org/10.1002/9781119156895.ch14

Turcotte, D. L., & Schubert, G. (2014). *Geodynamics* (3rd ed.). Cambridge University Press.

Vaughan, M. T., & Guggenheim, S. (1986). Elasticity of muscovite and its relationship to crystal structure. *Journal of Geophysical Research*, *91*(B5), 4657–4664. https://doi.org/10.1029/JB091iB05p04657

Vel, S. S., Cook, A. C., Johnson, S. E., & Gerbi, C. C. (2016). Computational homogenization and micromechanical analysis of textured polycrystalline materials. *Computer Methods in Applied Mechanics and Engineering*, *310*, 749–779. https://doi.org/10.1016/j.cma.2016.07.037

Walsh, J. B. (1965). The effect of cracks on the compressibility of rock. *Journal of Geophysical Research*, *70*(2), 381–389. https://doi.org/10.1029/JZ070i002p00381

Wang, C., & Ludman, A. (2004). Deformation conditions, kinematics, and displacement history of shallow crustal ductile shearing in the Norumbega fault system in the Northern

Appalachians, eastern Maine. *Tectonophysics*, *384*(1–4), 129–148. https://doi.org/10.1016/j.tecto.2004.03.013

Wang, D., & Mori, J. (2012). The 2010 Qinghai, China, earthquake: A moderate earthquake with supershear rupture. *Bulletin of the Seismological Society of America*, *102*(1), 301–308. https://doi.org/10.1785/0120110034

Ward, D., Mahan, K., & Schulte-Pelkum, V. (2012). Roles of quartz and mica in seismic anisotropy of mylonites. *Geophysical Journal International*, *190*(2), 1123–1134. https://doi.org/10.1111/j.1365-246X.2012.05528.x

Watling, B. (2017). *Seismic Anisotropy As A Function Of Mineralogy And Rock Type In Chester Gneiss Dome, Southeast Vermont* (Doctoral dissertation). Retrieved from https://digitalcommons.wayne.edu/oa_theses/593. Detroit, MI, USA: Wayne State University.

Weertman, J. (1980). Unstable slippage across a fault that separates elastic media of different elastic constants. *Journal of Geophysical Research*, *85*(B3), 1455–1461. https://doi.org/10.1029/JB085iB03p01455

Weertman, J. (2005). Slip event propagation direction in transition region of low surface slope. *Annals of Glaciology*, *40*(1), 43–46. https://doi.org/10.3189/172756405781813429

West, D. P., Jr. (1999). Timing of displacements along the Norumbega fault system, south-central and south-coastal Maine. In A. Ludman & D. P. West Jr. (Eds.), *Norumbega Fault System of the Northern Appalachians* (Vol. 331, pp. 167–178). Geological Society of America Special Paper 331. https://doi.org/10.1130/0-8137-2331-0.167

West, D. P., Jr., & Hubbard, M. S. (1997). Progressive localization of deformation during exhumation of a major strike-slip shear zone: Norumbega fault zone, south-central Maine, USA. *Tectonophysics*, *273*(3–4), 185–201. https://doi.org/10.1016/S0040-1951(96)00306-X

West, D. P., Jr., & Peterman, E. M. (2004). Bedrock geology of the Razorville Quadrangle, Maine. *Maine Geological Survey, Open-File Map 04-29*, color map, scale 1:24000. Retrieved from https://digitalmaine.com/mgs_maps/40/

Winterstein, D. F. (1990). Velocity anisotropy terminology for geophysicists. *Geophysics*, *55*(8), 1070–1088. https://doi.org/10.1190/1.1442919

Xia, K., Rosakis, A. J., & Kanamori, H. (2004). Laboratory earthquakes: the sub-Rayleigh-to-supershear rupture transition. *Science*. https://doi.org/10.1126/science.1094022

Xia, K., Rosakis, A. J., Kanamori, H., & Rice, J. R. (2005). Laboratory earthquakes along inhomogeneous faults: directionality and supershear. *Science*. https://doi.org/10.1126/science.1108193

Xu, S., & Ben-Zion, Y. (2017). Theoretical constraints on dynamic pulverization of fault zone rocks. *Geophysical Journal International*, *209*(1), 282–296. https://doi.org/10.1093/gji/ggx033

Yazdani, A., Nicknam, A., Dadras, E. Y., & Eftekhari, S. N. (2017). Near-Field Probabilistic Seismic Hazard Analysis of Metropolitan Tehran Using Region-Specific Directivity Models. *Pure and Applied Geophysics*, *174*(1), 117–132. https://doi.org/10.1007/s00024-016-1389-6

Yuan, F., Prakash, V., & Tullis, T. (2011). Origin of pulverized rocks during earthquake fault rupture. *Journal of Geophysical Research*, *116*(B6), B06309. https://doi.org/10.1029/2010JB007721

Yue, H., Lay, T., Freymueller, J. T., Ding, K., Rivera, L., Ruppert, N. A., & Koper, K. D. (2013). Supershear rupture of the 5 January 2013 Craig, Alaska (Mw 7.5) earthquake. *Journal of Geophysical Research*, *118*(11), 5903–5919. https://doi.org/10.1002/2013JB010594

Zhai, C., Li, C., Kunnath, S., & Wen, W. (2018). An efficient algorithm for identifying pulse-like ground motions based on significant velocity half-cycles. *Earthquake Engineering and Structural Dynamics*, *47*(3), 757–771. https://doi.org/10.1002/eqe.2989

Figure 1. Plan view illustration of seismic waves, particle velocities, and damage distributions generated by subshear rupture along right-lateral strike-slip faults in elastically isotropic media. (a) *P*- and *S*-wave fronts at a given time for a homogeneous isotropic interface between identical solids, showing symmetry with respect to the interface. Rupture is propagating in both directions (left and right). (b) *P*- and *S*-wave fronts at a given time for an isotropic bimaterial interface in stiff (upper block) and compliant (lower block) materials. The compliant block has slower *P*- and *S*-wave fronts (P_{slow} and S_{slow}, respectively) and two different head wave fronts (*P*-to-*P* between P_{fast} and P_{slow} and *S*-to-*S* between S_{fast} and S_{slow}). A wrinkle-like rupture pulse (small red bar within the black box) is propagating to the left. In (a) and (b), the left-propagating wave fronts (solid lines) are traced from the numerical simulations of particle velocities by Ben-Zion (2001), and the corresponding right-propagating wave fronts (dashed lines) are extrapolated from these results. (c) Enlarged view of the black box in (b) showing asymmetric particle velocities (black

arrows) near the rupture pulse. Note larger particle velocities in the more compliant material (below the interface) than in the stiffer material (above the interface). Consequently, dilation and compression occur near the rupture tips in the “positive” and “negative” directions, respectively (left and right sides of the red bar), allowing rupture propagation to the “positive” direction (the slip direction of the more compliant material). After Ben-Zion (2001) and Dor, Rockwell, et al. (2006). (d) Simplified schematic drawing of damage (fracture) distribution generated by a crack-like rupture in a homogeneous isotropic medium. Off-fault fractures are produced in both sides of the fault but on the tensile (T) rather than compressional (C) side of each rupture front, and generally oriented at high angles (70–80°) to the fault. Modified from Ben-Zion and Shi (2005), Griffith et al. (2009), and Okubo et al. (2019). (e) Simplified schematic drawing of damage (fracture) distribution generated by a wrinkle-like rupture propagating to the left in an isotropic bimaterial medium. Off-fault fractures are produced only in the tensile (T) quadrant on stiffer side of the fault and have little apparent preferred orientations. Modified from Ben-Zion and Shi (2005) and Xu and Ben-Zion (2017). Green stars in (a), (b), (d) and (e) indicate nucleation point.

Figure 2. Geologic setting and damage distribution of the Sandhill Corner shear zone (SCSZ) in the Norumbega fault system (NSF). (a) Regional geologic maps of the right-lateral NSF and SCSZ (red star). The SCSZ near the study area (red box) separates two lithologic units (Cape Elizabeth Formation and Crummett Mt. Formation). Modified from Price et al. (2016). CT, Connecticut; MA, Massachusetts; NH, New Hampshire; VT, Vermont. (b) Study area and two host rock sample locations (white circles; BB6 and 35) for the present study. Samples for analyses of microfracture density and fragment size distribution in (d) are also marked by black circles (B. R. Song et al., 2020). The core of the shear zone (ultramylonite) is the lithologic contact between quartzofeldspathic (QF) and schist units. (c) Foliation and lineation of the SCSZ (upper panel) and host rocks (lower panel) plotted by equal-area, lower hemisphere projection. Mean values (strike/dip and trend/plunge, respectively) of mylonitic foliation and stretching lineation in the SCSZ indicate a northeast-trending, subvertical, strike-slip fault/shear zone. The host rocks show mean foliation subparallel to that of the SCSZ. Data from Grover and Fernandes (2003), and West and Peterman (2004). (d) Plots of microfracture density (red squares) and three-dimensional *D*-value (blue circles) for garnet samples in (b) against perpendicular distance from the QF/schist lithologic contact (data from B. R. Song et al., 2020; negative distance

indicates the QF unit). The widths of effective damage zones are determined by the best fit lines above the background microfracture density. *D*-value is taken from the exponent of a power-law trend in the cumulative size distribution of garnet fragments. The widths of pulverized zones are determined by samples with *D*-value ≥ 2.5. Note highly asymmetric distribution of the effective damage and pulverized zones around the shear zone core.

Figure 3. Photomicrographs of two host rock samples cut perpendicular to the foliation and parallel to the lineation. (a) Quartzofeldspathic (QF) host rock (sample BB6) with lower mica content. (b) Schist host rock (sample 35) with higher mica content. Red boxes present the analysis regions by EBSD (see Figure 4a). XPL, cross-polarized light; PPL, plane-polarized light; Qz, quartz; Pl, plagioclase; Bt, biotite; Ms, muscovite; Grt, garnet. Dark gray vertical stripes in (b) are scratches on the slide glass.

Figure 4. Phase maps, *P*- (qV_{P}) and *S*-wave velocities (qV_{SH} and qV_{SV}), and velocity contrasts for the quartzofeldspathic (QF) and schist host rocks of the Sandhill Corner shear zone. (a) Phase maps of the analyzed QF (sample BB6) and schist (sample 35) host rocks by EBSD with lower (13.9 modal%) and higher (70.5 modal%) mica contents, respectively. Different shades of colors indicate different grains. See Figure 3 for analysis location. The coordinate system and azimuth ϕ (wave incidence angle) are also shown. (b) 2D qV_{P} for each rock plotted against azimuth ϕ from 0° to 180° in the $x1$-$x2$ plane. (c) qV_{P} contrast between the QF and schist rocks plotted against azimuth ϕ, calculated from (b). Shading indicates more compliant rock with lower velocity (red – QF; blue – schist). (d) 3D qV_{P} and its seismic anisotropy (AV_{P}) for each rock. (e) 2D qV_{SH} and qV_{SV} for each rock plotted against azimuth ϕ from 0° to 180° in the $x1$-$x2$ plane. (f) qV_{SH} and qV_{SV} contrasts between the QF and schist rocks plotted against azimuth ϕ, calculated from (e). (g) 3D qV_{SH} and its seismic anisotropy (AV_{SH}) for each rock. (h) 3D qV_{SV} and its seismic anisotropy (AV_{SV}) for each rock. 3D wave velocities in (d), (g) and (h) are presented in equal-area, upper hemisphere projection and with the same color limits for comparison.

Figure 5. Phase maps, *P*- (qV_{P}) and *S*-wave velocities (qV_{SH} and qV_{SV}), and velocity contrasts for synthetic rock samples with the same mica contents as the natural quartzofeldspathic (QF) and schist host rocks of the Sandhill Corner shear zone. (a) Phase maps of the synthetic QF and

schist rocks with lower (14.1 modal%) and higher (70.6 modal%) mica contents, respectively. Mica grains show a preferred orientation, but quartz and plagioclase grains are randomly oriented. The coordinate system and azimuth ϕ (wave incidence angle) are also presented. (b) 2D qV_{P} for each synthetic rock plotted against azimuth ϕ from 0° to 180° in the $x1$-$x2$ plane. (c) qV_{P} contrast between the synthetic QF and schist rocks plotted against azimuth ϕ, calculated from (b). Shading indicates more compliant rock with lower velocity (red – QF; blue – schist). (d) 3D qV_{P} and its seismic anisotropy (AV_{P}) for each synthetic rock. (e) 2D qV_{SH} and qV_{SV} for each synthetic rock plotted against azimuth ϕ from 0° to 180° in the $x1$-$x2$ plane. (f) qV_{SH} and qV_{SV} contrasts between the synthetic QF and schist rocks plotted against azimuth ϕ, calculated from (e). (g) 3D qV_{SH} and its seismic anisotropy (AV_{SH}) for each synthetic rock. (h) 3D qV_{SV} and its seismic anisotropy (AV_{SV}) for each synthetic rock. 3D wave velocities in (d), (g) and (h) are presented in equal-area, upper hemisphere projection and with the same color limits for comparison.

Figure 6. Polar plots of 2D seismic velocities (qV_{P}, qV_{SH} and qV_{SV}) in the $x1$-$x2$ plane for quartzofeldspathic (QF; upper half) and schist (lower half) rocks. (a) Natural QF and schist host rocks of the Sandhill Corner shear zone (SCSZ). (b) Synthetic QF and schist rocks. These are the same as the velocity graphs plotted in rectangular coordinates (Figures 4b, 4e, 5b and 5e), but these plots in polar coordinates can be considered as plan view of seismic waves at a unit time for QF and schist rocks across the lithologic contact (fault), highlighting how velocity changes with direction in an anisotropic medium.

Figure 7. Effect of mica content, in synthetic rocks, on seismic velocity, anisotropy, and velocity contrast relative to the synthetic quartzofeldspathic (QF) rock. (a) Phase maps of selected synthetic microstructures with mica contents from 0% to 100% in 20% intervals. See Figure S7 for the full dataset (10% intervals). Each phase map with mica has the same ratio of biotite and muscovite (Bt:Ms = 50:50). The coordinate system and phase color information are also shown. (b) 2D seismic velocities of *P*, *SH* and *SV* waves for each synthetic microstructure in (a) plotted against azimuth ϕ (wave incidence angle) from 0° to 180° in the $x1$-$x2$ plane. See Figure S7 for the full dataset (10% intervals). The velocities for the synthetic QF (black dashed line) and schist (black dotted line) rocks are also plotted. (c) Seismic anisotropies of *P* and *SH* waves (AV_{P} and AV_{SH}, respectively) for the full dataset of synthetic microstructures, plotted against mica content.

SV-wave seismic anisotropy is similar to AV_{SH} (see Figure S7). Open squares and triangles indicate the synthetic QF and schist rocks, respectively (Figures 5d and g). Seismic anisotropies for single crystals of quartz, plagioclase, biotite (phlogopite) and muscovite are also plotted. (d) Velocity contrasts at $\phi = 0°$ for the full dataset of synthetic microstructures relative to the synthetic QF rock plotted against mica content. Open triangles indicate the synthetic schist (Figures 5c and f). Shading indicates the ranges of more compliant rocks with lower velocities than the synthetic QF rock at $\phi = 0°$. In (c) and (d), three types of results are plotted where relative modal percentages of biotite and muscovite are 100:0 (dashed line), 50:50 (solid line), and 0:100 (dotted line).

Figure 8. Comparison of seismic anisotropy and velocity contrast for natural rocks from the literature, obtained by petrophysical measurements and EBSD analysis (see Table S2 for details). Common felsic to intermediate rocks in the middle crust with different mica content are compared (schist, gneiss, mylonite, quartzite, and igneous rocks such as granite), in which quartz, feldspars, biotite and muscovite comprise >~90 modal%. (a) 3D *P*-wave seismic anisotropy (AV_P) for 135 rock samples (2 from the present study and 133 from the literature), plotted against mica content. Open black square and triangle indicate the quartzofeldspathic (QF) and schist host rocks of the Sandhill Corner shear zone (SCSZ), respectively. AV_P of synthetic rocks (black lines) are overlaid for reference. AV_P of the natural rocks show a general increase with more mica content, similar to the synthetic rocks. (b) *SH*-wave velocity (qV_{SH}) contrast at $\phi = 0°$ for 30 rock samples (1 from the present study and 29 from the literature) relative to the natural SCSZ QF host rock (sample BB6), plotted against mica content. Open red triangle indicates the SCSZ schist host rock (sample 35). qV_{SH} contrast of synthetic rocks (red lines) are overlaid for reference. qV_{SH} contrasts of the natural rocks relative to the SCSZ QF host rock show a general increase with lower and higher mica content than the SCSZ QF host rock, similar to the synthetic rocks. The rocks with more mica content than the SCSZ QF host rock (13.9 modal%) are more compliant for qV_{SH} at $\phi = 0°$, which is also generally consistent with the synthetic rocks (shading).

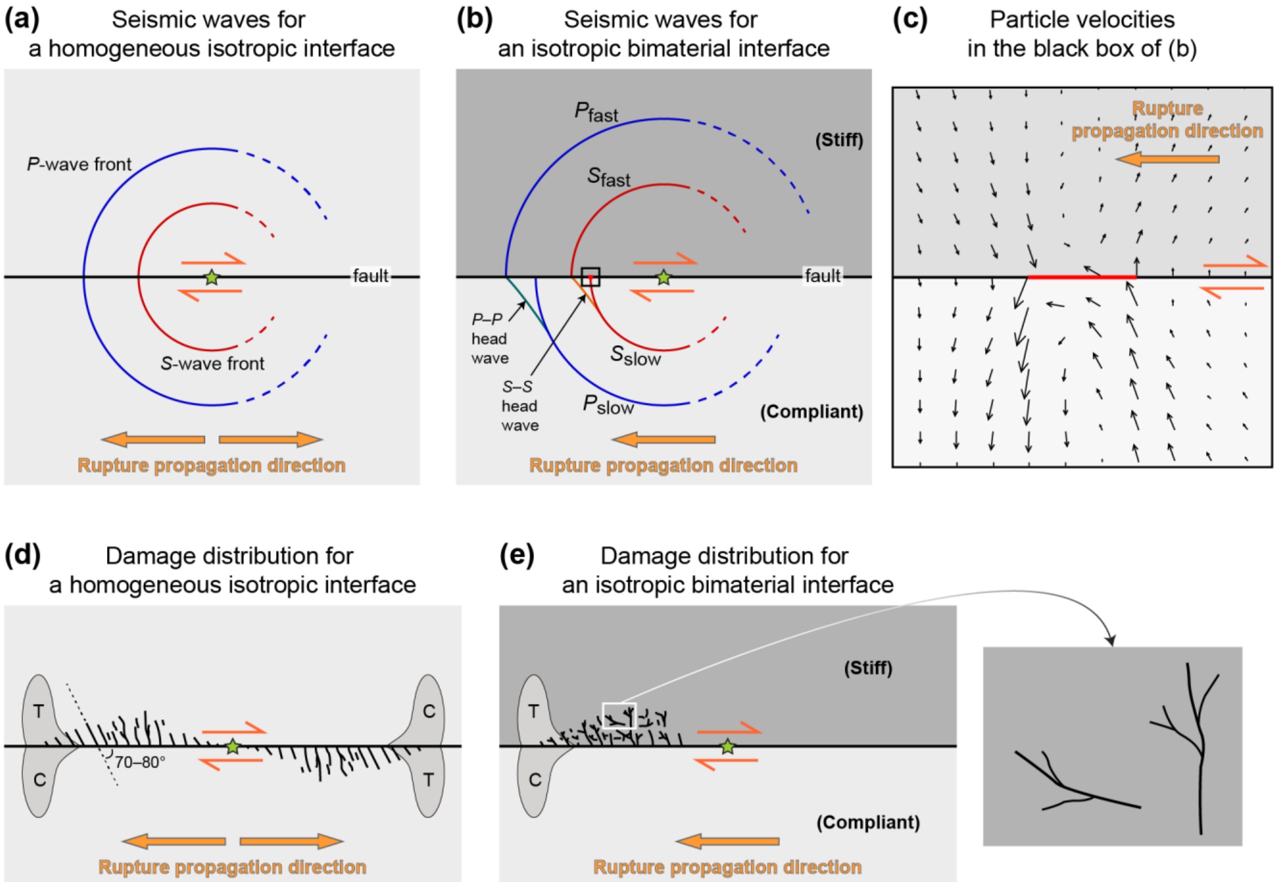

Figure 1. Plan view illustration of seismic waves, particle velocities, and damage distributions generated by subshear rupture along right-lateral strike-slip faults in elastically isotropic media. (a) *P*- and *S*-wave fronts at a given time for a homogeneous isotropic interface between identical solids, showing symmetry with respect to the interface. Rupture is propagating in both directions (left and right). (b) *P*- and *S*-wave fronts at a given time for an isotropic bimaterial interface in stiff (upper block) and compliant (lower block) materials. The compliant block has slower *P*- and *S*-wave fronts (P_{slow} and S_{slow}, respectively) and two different head wave fronts (*P*-to-*P* between P_{fast} and P_{slow} and *S*-to-*S* between S_{fast} and S_{slow}). A wrinkle-like rupture pulse (small red bar within the black box) is propagating to the left. In (a) and (b), the left-propagating wave fronts (solid lines) are traced from the numerical simulations of particle velocities by Ben-Zion (2001), and the corresponding right-propagating wave fronts (dashed lines) are extrapolated from these results. (c) Enlarged view of the black box in (b) showing asymmetric particle velocities (black arrows) near the rupture pulse. Note larger particle velocities in the more compliant material (below the interface) than in the stiffer material (above the interface). Consequently, dilation and compression occur near the rupture tips in the "positive" and "negative" directions, respectively (left and right sides of the red bar), allowing rupture propagation to the "positive" direction (the slip direction of the more compliant material). After Ben-Zion (2001) and Dor, Rockwell, et al. (2006). (d) Simplified schematic drawing of damage (fracture) distribution generated by a crack-like rupture in a homogeneous isotropic medium. Off-fault fractures are produced in both sides of the fault but on the tensile (T) rather than compressional (C) side of each rupture front, and generally oriented at high angles (70–80°) to the fault. Modified from Ben-Zion and Shi (2005), Griffith et al. (2009), and Okubo et al. (2019). (e) Simplified schematic drawing of damage (fracture) distribution generated by a wrinkle-like rupture propagating to the left in an isotropic bimaterial medium. Off-fault fractures are produced only in the tensile (T) quadrant on stiffer side of the fault and have little apparent preferred orientations. Modified from Ben-Zion and Shi (2005) and Xu and Ben-Zion (2017). Green stars in (a), (b), (d) and (e) indicate nucleation point.

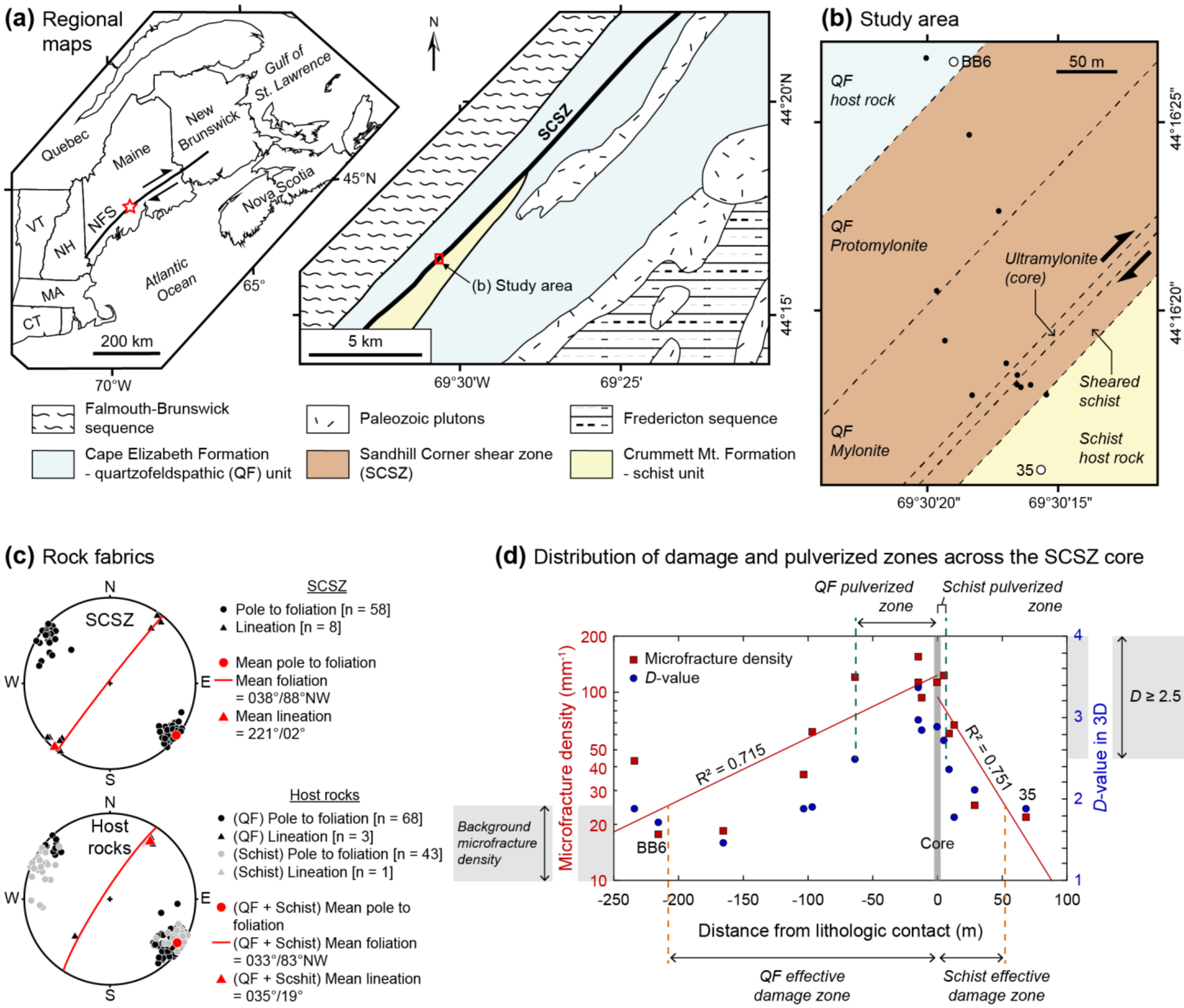

Figure 2. Geologic setting and damage distribution of the Sandhill Corner shear zone (SCSZ) in the Norumbega fault system (NSF). (a) Regional geologic maps of the right-lateral NSF and SCSZ (red star). The SCSZ near the study area (red box) separates two lithologic units (Cape Elizabeth Formation and Crummett Mt. Formation). Modified from Price et al. (2016). CT, Connecticut; MA, Massachusetts; NH, New Hampshire; VT, Vermont. (b) Study area and two host rock sample locations (white circles; BB6 and 35) for the present study. Samples for analyses of microfracture density and fragment size distribution in (d) are also marked by black circles (B. R. Song et al., 2020). The core of the shear zone (ultramylonite) is the lithologic contact between quartzofeldspathic (QF) and schist units. (c) Foliation and lineation of the SCSZ (upper panel) and host rocks (lower panel) plotted by equal-area, lower hemisphere projection. Mean values (strike/dip and trend/plunge, respectively) of mylonitic foliation and stretching lineation in the SCSZ indicate a northeast-trending, subvertical, strike-slip fault/shear zone. The host rocks show mean foliation subparallel to that of the SCSZ. Data from Grover and Fernandes (2003), and West and Peterman (2004). (d) Plots of microfracture density (red squares) and three-dimensional *D*-value (blue circles) for garnet samples in (b) against perpendicular distance from the QF/schist lithologic contact (data from B. R. Song et al., 2020; negative distance indicates the QF unit). The widths of effective damage zones are determined by the best fit lines above the background microfracture density. *D*-value is taken from the exponent of a power-law trend in the cumulative size distribution of garnet fragments. The widths of pulverized zones are determined by samples with *D*-value ≥ 2.5. Note highly asymmetric distribution of the effective damage and pulverized zones around the shear zone core.

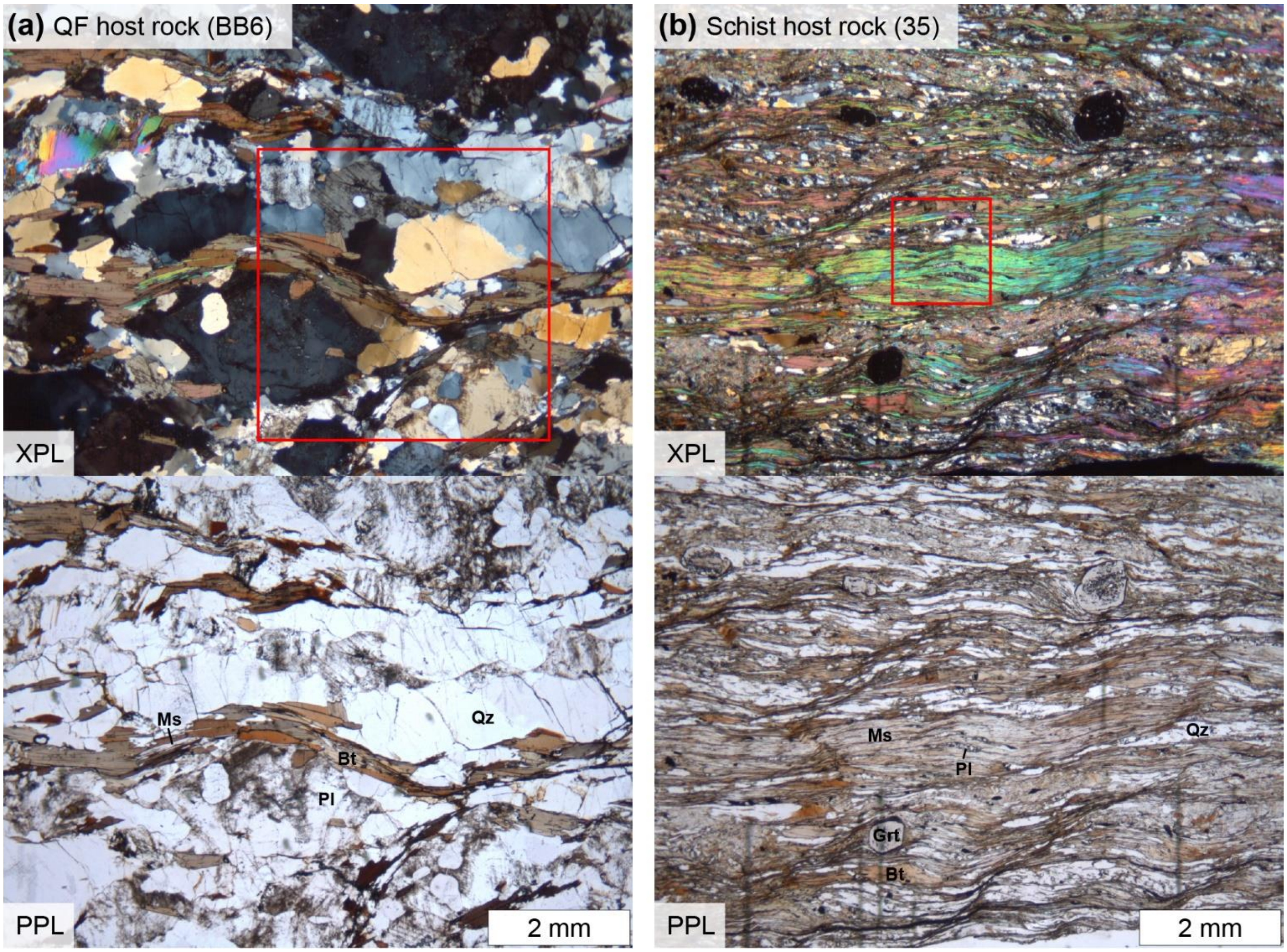

Figure 3. Photomicrographs of two host rock samples cut perpendicular to the foliation and parallel to the lineation. (a) Quartzofeldspathic (QF) host rock (sample BB6) with lower mica content. (b) Schist host rock (sample 35) with higher mica content. Red boxes present the analysis regions by EBSD (see Figure 4a). XPL, cross-polarized light; PPL, plane-polarized light; Qz, quartz; Pl, plagioclase; Bt, biotite; Ms, muscovite; Grt, garnet. Dark gray vertical stripes in (b) are scratches on the slide glass.

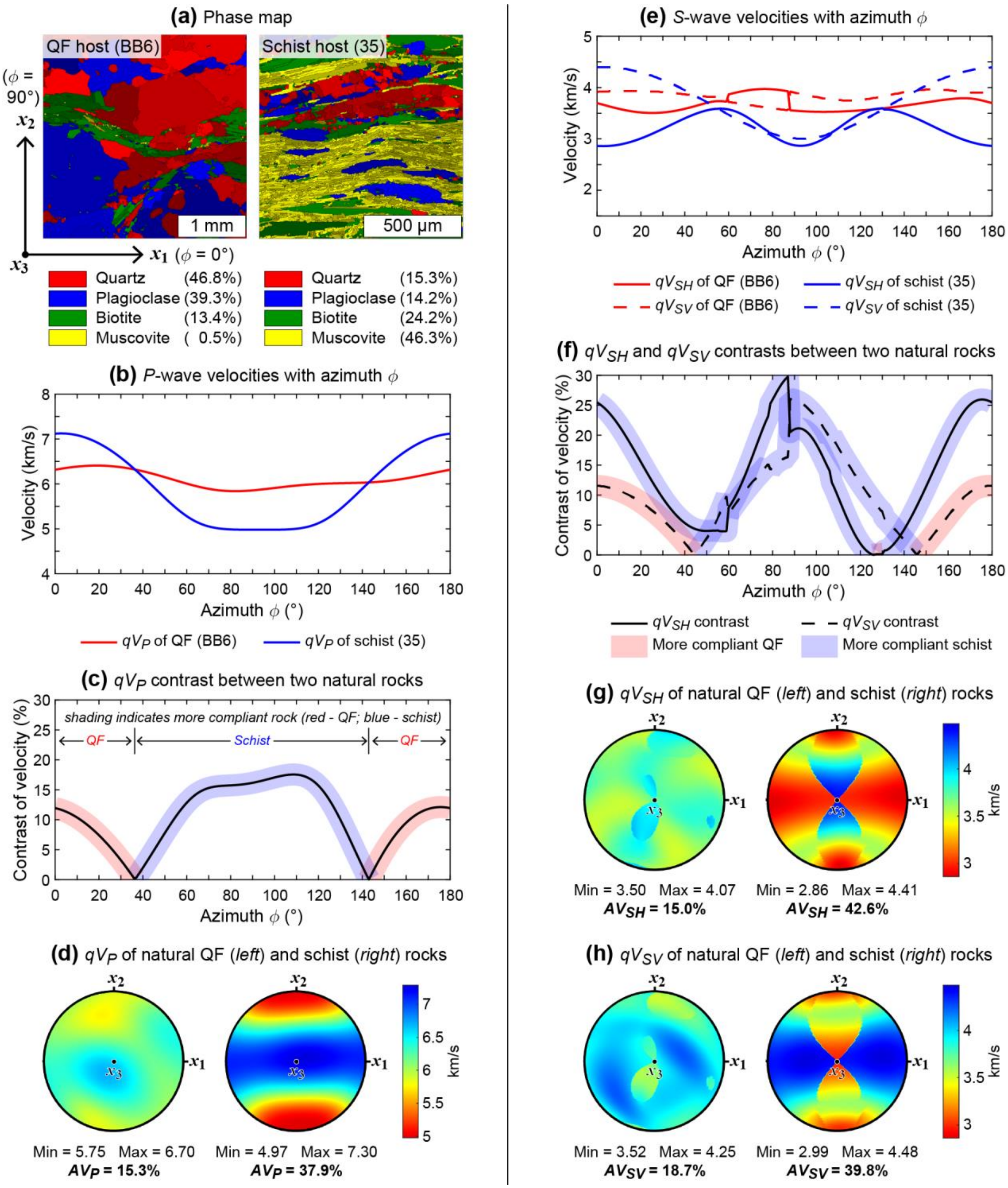

Figure 4. Phase maps, *P*- (qV_P) and *S*-wave velocities (qV_{SH} and qV_{SV}), and velocity contrasts for the quartzofeldspathic (QF) and schist host rocks of the Sandhill Corner shear zone. (a) Phase maps of the analyzed QF (sample BB6) and schist (sample 35) host rocks by EBSD with lower (13.9 modal%) and higher (70.5 modal%) mica contents, respectively. Different shades of colors indicate different grains. See Figure 3 for analysis location. The coordinate system and azimuth ϕ (wave incidence angle) are also shown. (b) 2D qV_P for each rock plotted against azimuth ϕ from 0° to 180° in the $x1$-$x2$ plane. (c) qV_P contrast between the QF and schist rocks plotted against azimuth ϕ, calculated from (b). Shading indicates more compliant rock with lower velocity (red – QF; blue – schist). (d) 3D qV_P and its seismic anisotropy (AV_P) for each rock. (e) 2D qV_{SH} and qV_{SV} for each rock plotted against azimuth ϕ from 0° to 180° in the $x1$-$x2$ plane. (f) qV_{SH} and qV_{SV} contrasts between the QF and schist rocks plotted against azimuth ϕ, calculated from (e). (g) 3D qV_{SH} and its seismic anisotropy (AV_{SH}) for each rock. (h) 3D qV_{SV} and its seismic anisotropy (AV_{SV}) for each rock. 3D wave velocities in (d), (g) and (h) are presented in equal-area, upper hemisphere projection and with the same color limits for comparison.

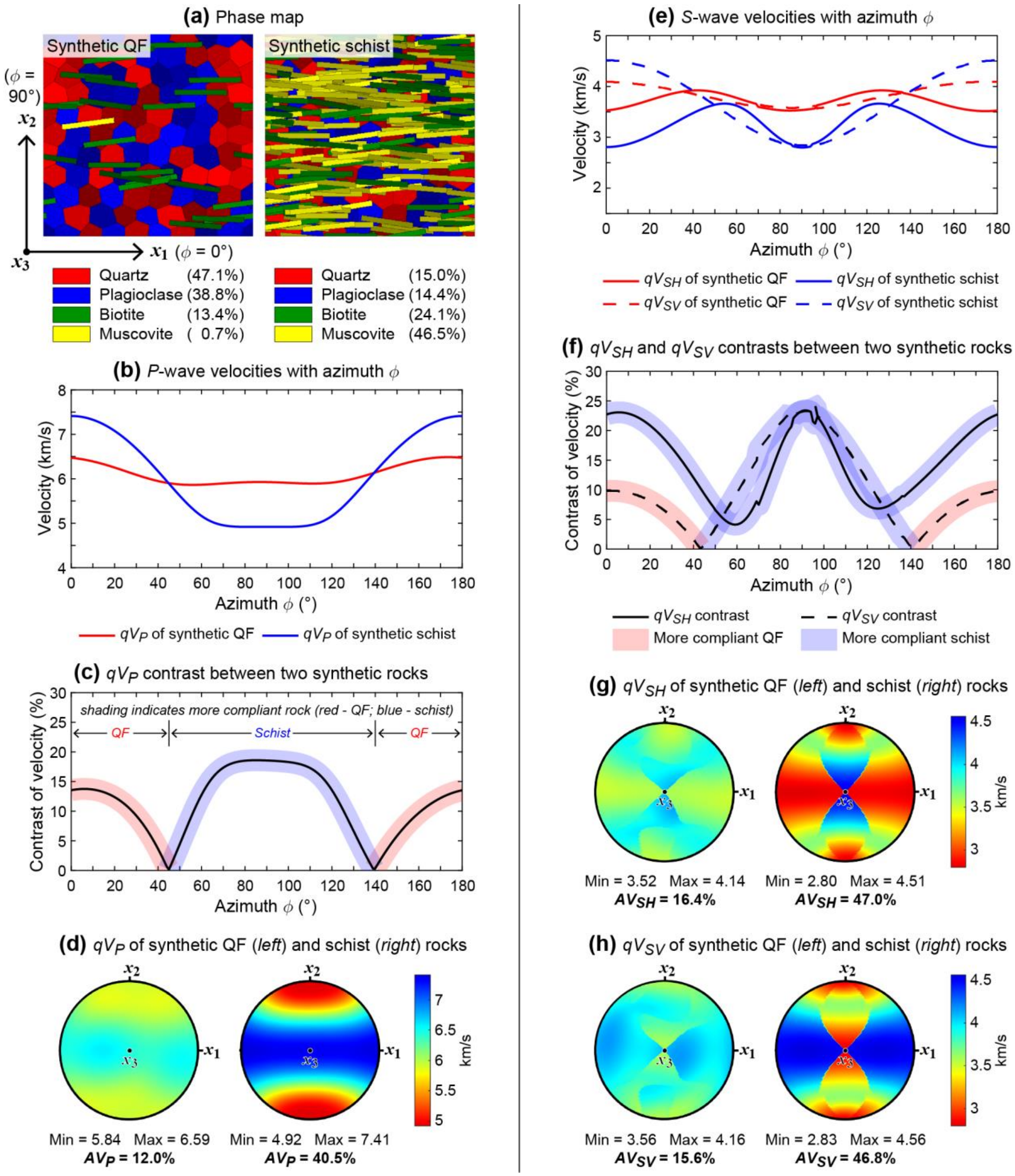

Figure 5. Phase maps, *P*- (qV_P) and *S*-wave velocities (qV_{SH} and qV_{SV}), and velocity contrasts for synthetic rock samples with the same mica contents as the natural quartzofeldspathic (QF) and schist host rocks of the Sandhill Corner shear zone. (a) Phase maps of the synthetic QF and schist rocks with lower (14.1 modal%) and higher (70.6 modal%) mica contents, respectively. Mica grains show a preferred orientation, but quartz and plagioclase grains are randomly oriented. The coordinate system and azimuth ϕ (wave incidence angle) are also presented. (b) 2D qV_P for each synthetic rock plotted against azimuth ϕ from 0° to 180° in the *x*1-*x*2 plane. (c) qV_P contrast between the synthetic QF and schist rocks plotted against azimuth ϕ, calculated from (b). Shading indicates more compliant rock with lower velocity (red – QF; blue – schist). (d) 3D qV_P and its seismic anisotropy (AV_P) for each synthetic rock. (e) 2D qV_{SH} and qV_{SV} for each synthetic rock plotted against azimuth ϕ from 0° to 180° in the *x*1-*x*2 plane. (f) qV_{SH} and qV_{SV} contrasts between the synthetic QF and schist rocks plotted against azimuth ϕ, calculated from (e). (g) 3D qV_{SH} and its seismic anisotropy (AV_{SH}) for each synthetic rock. (h) 3D qV_{SV} and its seismic anisotropy (AV_{SV}) for each synthetic rock. 3D wave velocities in (d), (g) and (h) are presented in equal-area, upper hemisphere projection and with the same color limits for comparison.

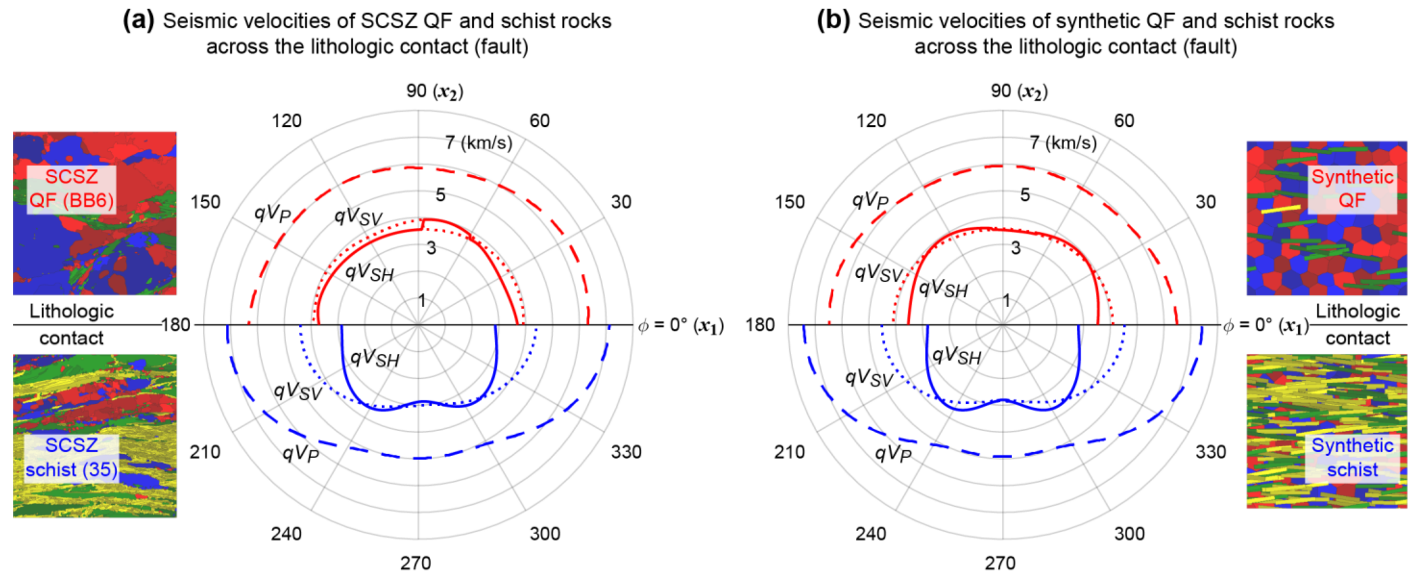

Figure 6. Polar plots of 2D seismic velocities (qV_P, qV_{SH} and qV_{SV}) in the $x1$-$x2$ plane for quartzofeldspathic (QF; upper half) and schist (lower half) rocks. (a) Natural QF and schist host rocks of the Sandhill Corner shear zone (SCSZ). (b) Synthetic QF and schist rocks. These are the same as the velocity graphs plotted in rectangular coordinates (Figures 4b, 4e, 5b and 5e), but these plots in polar coordinates can be considered as plan view of seismic waves at a unit time for QF and schist rocks across the lithologic contact (fault), highlighting how velocity changes with direction in an anisotropic medium.

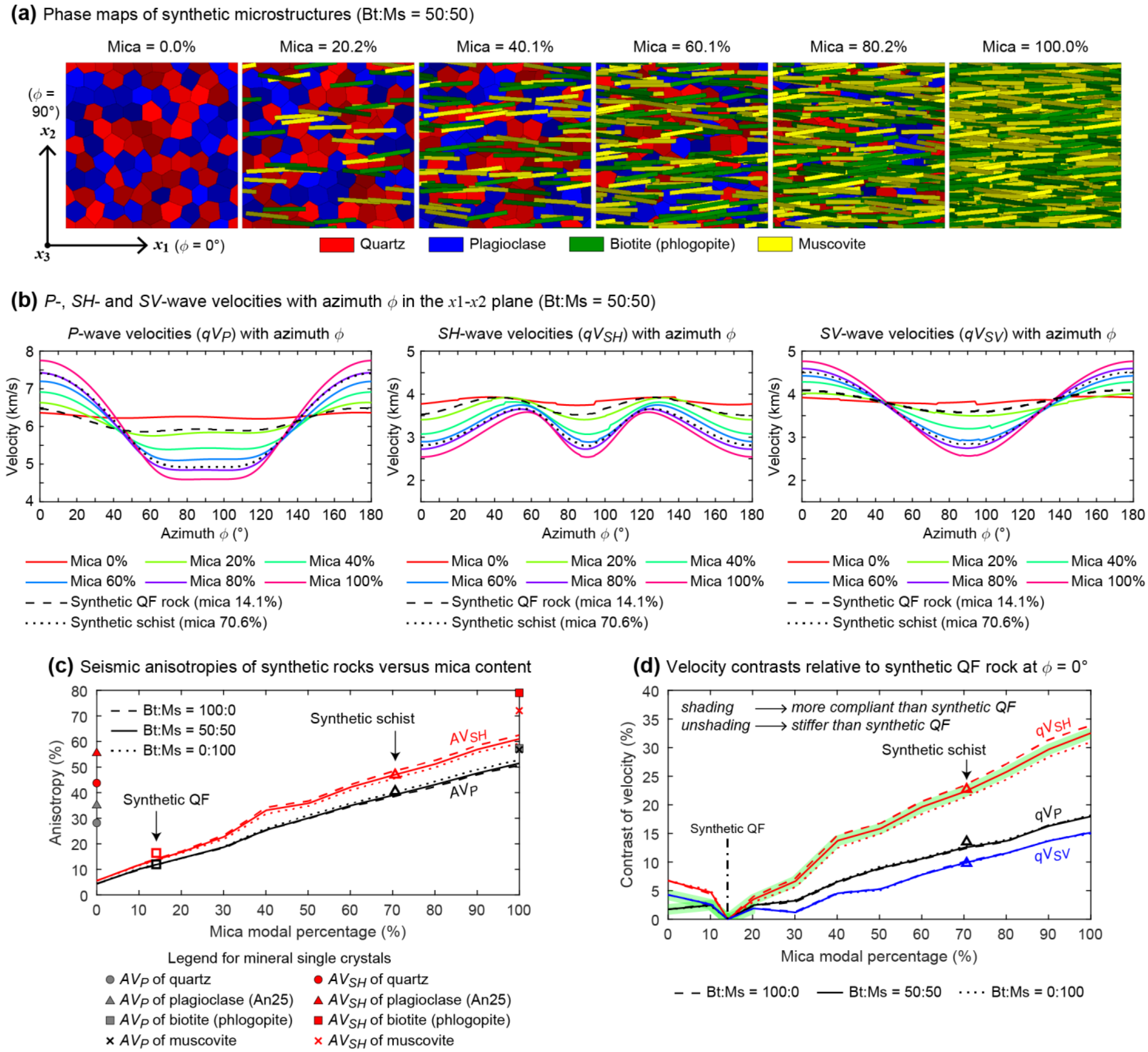

Figure 7. Effect of mica content, in synthetic rocks, on seismic velocity, anisotropy, and velocity contrast relative to the synthetic quartzofeldspathic (QF) rock. (a) Phase maps of selected synthetic microstructures with mica contents from 0% to 100% in 20% intervals. See Figure S7 for the full dataset (10% intervals). Each phase map with mica has the same ratio of biotite and muscovite (Bt:Ms = 50:50). The coordinate system and phase color information are also shown. (b) 2D seismic velocities of *P*, *SH* and *SV* waves for each synthetic microstructure in (a) plotted against azimuth ϕ (wave incidence angle) from 0° to 180° in the $x1$-$x2$ plane. See Figure S7 for the full dataset (10% intervals). The velocities for the synthetic QF (black dashed line) and schist (black dotted line) rocks are also plotted. (c) Seismic anisotropies of *P* and *SH* waves (AV_P and AV_{SH}, respectively) for the full dataset of synthetic microstructures, plotted against mica content. *SV*-wave seismic anisotropy is similar to AV_{SH} (see Figure S7). Open squares and triangles indicate the synthetic QF and schist rocks, respectively (Figures 5d and g). Seismic anisotropies for single crystals of quartz, plagioclase, biotite (phlogopite) and muscovite are also plotted. (d) Velocity contrasts at ϕ = 0° for the full dataset of synthetic microstructures relative to the synthetic QF rock plotted against mica content. Open triangles indicate the synthetic schist (Figures 5c and f). Shading indicates the ranges of more compliant rocks with lower velocities than the synthetic QF rock at ϕ = 0°. In (c) and (d), three types of results are plotted where relative modal percentages of biotite and muscovite are 100:0 (dashed line), 50:50 (solid line), and 0:100 (dotted line).

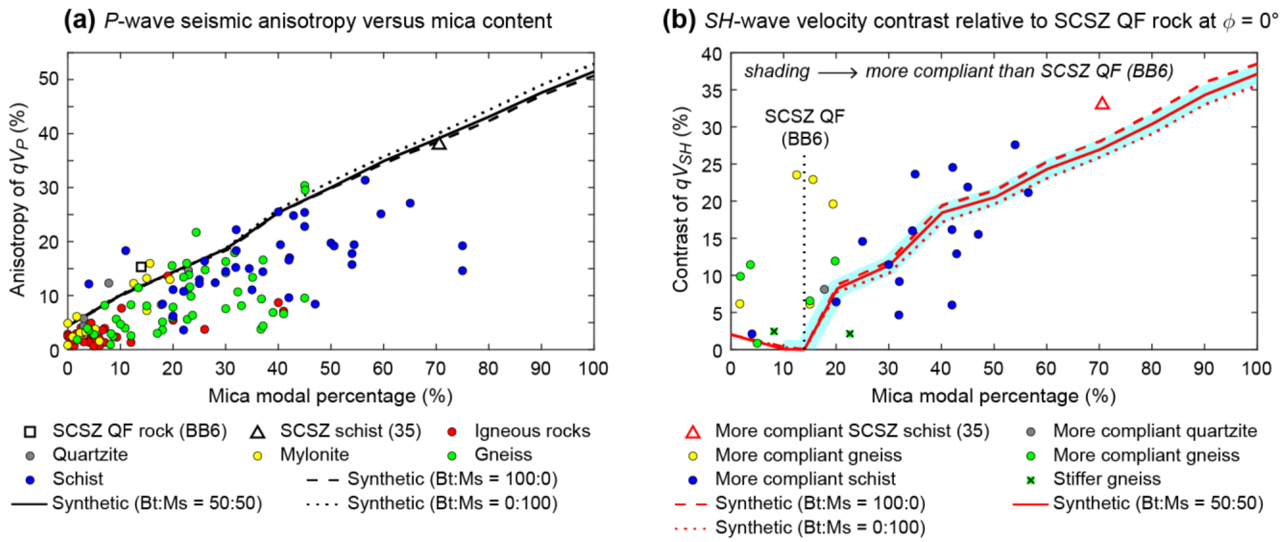

Figure 8. Comparison of seismic anisotropy and velocity contrast for natural rocks from the literature, obtained by petrophysical measurements and EBSD analysis (see Table S2 for details). Common felsic to intermediate rocks in the middle crust with different mica content are compared (schist, gneiss, mylonite, quartzite, and igneous rocks such as granite), in which quartz, feldspars, biotite and muscovite comprise >~90 modal%. (a) 3D *P*-wave seismic anisotropy (AV_P) for 135 rock samples (2 from the present study and 133 from the literature), plotted against mica content. Open black square and triangle indicate the quartzofeldspathic (QF) and schist host rocks of the Sandhill Corner shear zone (SCSZ), respectively. AV_P of synthetic rocks (black lines) are overlaid for reference. AV_P of the natural rocks show a general increase with more mica content, similar to the synthetic rocks. (b) *SH*-wave velocity (qV_{SH}) contrast at $\phi = 0°$ for 30 rock samples (1 from the present study and 29 from the literature) relative to the natural SCSZ QF host rock (sample BB6), plotted against mica content. Open red triangle indicates the SCSZ schist host rock (sample 35). qV_{SH} contrast of synthetic rocks (red lines) are overlaid for reference. qV_{SH} contrasts of the natural rocks relative to the SCSZ QF host rock show a general increase with lower and higher mica content than the SCSZ QF host rock, similar to the synthetic rocks. The rocks with more mica content than the SCSZ QF host rock (13.9 modal%) are more compliant for qV_{SH} at $\phi = 0°$, which is also generally consistent with the synthetic rocks (shading).